

# Laser ablation aerosol particle time-of-flight mass spectrometer (LAAPTOF): Performance, reference spectra and classification of atmospheric samples

Xiaoli Shen<sup>1,2</sup>, Ramakrishna Ramisetty<sup>1</sup>, Claudia Mohr<sup>1,3</sup>, Wei Huang<sup>1,2</sup>, Thomas Leisner<sup>1</sup>, Harald Saathoff<sup>1,\*</sup>

<sup>1</sup>Institute of Meteorology and Climate Research (IMK-AAF), Karlsruhe Institute of Technology (KIT), Hermann-von-Helmholtz-Platz 1, 76344 Eggenstein-Leopoldshafen, Germany

<sup>2</sup>Institute of Geography and Geoecology (IfGG), Karlsruhe Institute of Technology (KIT), Kaiserstr.12, 76131 Karlsruhe, Germany

<sup>3</sup>Now at: Department of Environmental Science and Analytical Chemistry, Stockholm University, Stockholm, 11418, Sweden

\*Correspondence to: Harald Saathoff ([harald.saathoff@kit.edu](mailto:harald.saathoff@kit.edu))

**Abstract.** The laser ablation aerosol particles time-of-flight mass spectrometer (LAAPTOF, Aeromegt GmbH) is able to identify the chemical composition and mixing state of individual aerosol particles, and thus is a tool for elucidating their impacts on human health, visibility, ecosystem and climate. The overall detection efficiency (ODE) of the instrument we use was determined to range from  $\sim(0.01 \pm 0.01)\%$  to  $\sim(6.574.23 \pm 2.3836)\%$  for polystyrene latex (PSL); in the size range of 200 to 2000 nm,  $\sim(0.44 \pm 0.19)\%$  to  $\sim(6.57 \pm 2.38)\%$  for ammonium nitrate ( $\text{NH}_4\text{NO}_3$ ), and  $\sim(0.14 \pm 0.02)\%$  to  $\sim(1.46 \pm 0.08)\%$  for sodium chloride (NaCl) particles in the size range of 300 to 1000 nm in the size range of 200 to 2000 nm. Reference mass spectra of 32 different particle types relevant for atmospheric aerosol (e.g. pure compounds  $\text{NH}_4\text{NO}_3$ ,  $\text{K}_2\text{SO}_4$ , NaCl, oxalic acid, pinic acid, and pinonic acid; internal mixtures of e.g. salts, secondary organic aerosol, and metallic core-organic shell particles; more complex particles such as soot and dust particles) were determined. Our results show that internally mixed aerosol particles can result in spectra with new clusters of ions, rather than simply a combination of the spectra from the single components. An exemplary one-day ambient data set was analysed by both classical Fuzzy clustering and a reference spectra based classification method. Resulting identified particle types were generally well correlated. We show how a combination of both methods can greatly improve the interpretation of single particle data in field measurements.~~An exemplary one-day ambient data set was analysed by both classical Fuzzy clustering and a reference spectra based classification method, generating results (Pearson's correlation coefficients of 0.76 to 0.95) with complementary advantages. Identifying main particle types without reference by Fuzzy clustering and identifying target particle types even with little abundance and potential sources by reference spectra based classification improved the interpretation of field measurements significantly.~~ leading to six different particle classes. Correlating these particle classes with the reference spectra as well as direct comparison of the ambient data with the reference spectra has proven how useful they are for the interpretation of field measurements, for e.g. grouping data, and identifying special particle types and potential sources.

## 1 Introduction

Atmospheric aerosol particles impact visibility, interact with trace gases, can act as cloud condensation and ice nuclei, and influence the Earth's radiation budget (Seinfeld and Pandis, 2006). Especially the continuously evolving chemical composition of aerosol particles is of scientific interest, as it influences all aerosol effects (Burkholder et al., 2017; Pöschl, 2005). However,

37 large knowledge gaps still exist related to the chemical composition of the organic and inorganic components and their mutual  
38 interaction (Jimenez et al., 2009; Murphy et al., 2006; Schill and Tolbert, 2013; Zhang et al., 2007).

39 Aerosol particles can contain various components ranging from volatile (e.g. nitrate, sulphate, ammonium salts, and many  
40 organic compounds), to refractory species (e.g. elemental carbon, minerals, and sea salt) (Pratt and Prather, 2012). The global  
41 aerosol mass burden was estimated to consist of 73.6% dust, 16.7% sea salt, 2.8% biogenic secondary organic aerosols (SOA),  
42 2.3% primary organic aerosols (POA), 1.3% sulphate, 1.3% ammonium, 1.2% nitrate, 0.4% black carbon (soot), 0.2%  
43 anthropogenic SOA, and 0.2% methane sulphonic acid (Tsigaridis et al., 2006). ~~SOA is estimated to account for the major~~  
44 ~~fraction of the total organic aerosol mass with dicarboxylic acids, such as oxalic acid suggested to be the main contributors~~  
45 ~~(Ervens et al., 2004). Ambient aerosols, either directly emitted (primary aerosols) or formed in the atmosphere (secondary~~  
46 ~~aerosols) from oxidation of gas phase precursors or chemical reactions on particles, have typical lifetimes ranging from hours to~~  
47 ~~a few weeks (Pöschl, 2005). During their the lifetime ambient aerosols' lifetime, ranging from hours to a few weeks (Pöschl,~~  
48 ~~2005), the complexity of their chemical composition usually increases by coagulation, cloud processing, and or chemical~~  
49 ~~reactions. Sea salt, POA, soot, or dust particles can e.g. heterogeneously react with secondary organic compounds like organic~~  
50 ~~acids and secondary inorganic compounds like sulfuric or nitric acid (Seinfeld and Pandis, 2006; Usher et al., 2003). This~~  
51 ~~modifies the particles' mixing state, with both internal (individual particles consisting of mixed compounds, e.g. coating~~  
52 ~~structures) and external mixtures (e.g. mixture of particles consisting of different compounds) (Li et al., 2016). This-The~~  
53 ~~forementioned findings underscores the importance of measuring aerosol chemical composition and its changes on short~~  
54 ~~timescales and on a single particle basis, which can be realized by on-line mass spectrometry.~~

55 One-line mass spectrometry includes bulk and single-particle measurements (Pratt and Prather, 2012). Single particle mass  
56 spectrometry, which can be dated back to the 1970s, aims at in situ and real time identification of the chemical composition of  
57 individual aerosol particles, hereby elucidating a particle's external and internal mixing properties (Noble and Prather, 2000).  
58 Online single particle mass spectrometers (SPMS) commonly use pulsed lasers for particle desorption and ionization (LDI), with  
59 the advantage of ionizing nearly all atmospheric particle components, including both non-refractory and refractory materials  
60 (Kulkarni et al., 2011). To the best of our knowledge, so far ~~there is no quantitative analysis of particle composition by SPMS~~  
61 ~~SPMS analysis is yet capable of providing a quantitative composition analysis~~, since the ablation/ionization laser cannot interact  
62 with the entire particle; and the ~~resulting-generated~~ ion fragments and/ clusters are susceptible to matrix effects (Ramisetty et al.,  
63 2017). In addition, ionization mechanisms are not fully understood (Murphy, 2007). ~~The first commercial SPMS combined LDI~~  
64 ~~with a Time of Flight Mass Spectrometer (aerosol time of flight mass spectrometer, ATOFMS, TSI GmbH) (Gard et al., 1997;~~  
65 ~~Su et al., 2004). Several other home build research SPMS were developed, each with different advantages: Particle Analysis by~~  
66 ~~Laser Mass Spectrometry (PALMS) (Brands et al., 2011; Erdmann et al., 2005; Gaie Levrel et al., 2012; Murphy, 2007; Murphy~~  
67 ~~and Thomson, 1995; Trimborn et al., 2000; Zelenyuk and Imre, 2005; Zelenyuk et al., 2009), Laser Mass Analyser for Particles~~  
68 ~~in the Airborne State (LAMPAS) (Trimborn et al., 2000), Single Particle Analysis and Sizing System (SPASS) (Erdmann et al.,~~  
69 ~~2005), Single Particle Laser Ablation Time of Flight Mass Spectrometer (SPLAT) (Zelenyuk and Imre, 2005; Zelenyuk et al.,~~  
70 ~~2009), Aircraft-based Laser Ablation Aerosol Mass spectrometer (ALABAMA) (Brands et al., 2011), and Single Particle Laser~~  
71 ~~Ablation Mass Spectrometer (SPLAM) (Gaie Levrel et al., 2012) to name some of them.~~ SPMS have identified many different  
72 ambient particle types in different regions of the atmosphere, such as an elemental carbon/organic carbon (ECOC), organic-  
73 sulphate, aged sea salt, biological, soil dust, and different metal dominated types (Dall'Osto et al., 2016; Moffet et al., 2008;  
74 Murphy et al., 2006; Schmidt et al., 2017). These measurements all confirmed the complexity of individual particles' mixing  
75 state, and demonstrated the usefulness of single particle mass spectra for apportionment of individual particle sources, including  
76 e.g. fossil fuel and biomass burning combustion, cooking, marine, and shipping sources (Arndt et al., 2016; Schmidt et al., 2017).

Feldfunktion geändert

Feldfunktion geändert

Feldfunktion geändert

77 Currently, there are only two commercially available SPMSs, i.e. the Single Particle Aerosol Mass Spectrometer (SPAMS,  
78 Hexin Analytical Instrument Co., Ltd., China) (Li et al., 2011; Lin et al., 2017) and the Laser Ablation Aerosol Particles Time-  
79 of-Flight mass spectrometer (LAAPTOF, Aeromegt GmbH, Germany). LAAPTOF uses two laser diodes (wave length 405  
80 nm, ~40 mW, ~50  $\mu$ m beam spot diameter) (wave length 405 nm, ~40 mW, ~50  $\mu$ m beam spot diameter, Marsden et al., 2016;  
81 Zawadowicz et al., 2017) for optical counting and size recording by light scattering, and one excimer laser (ArF, 193 nm, ~ 4  
82 mJ) for one step ablation/ionization. The overall detection efficiency (ODE) of this instrument, defined as the number of single  
83 particle mass spectra obtained from the total number of aerosol particles in the sampled air, was determined to range from ~0.15%  
84 to ~2.2% for polystyrene latex (PSL) particles with geometric diameters ( $d_p$ ) between 350 nm and 800 nm (Gemayel et al., 2016;  
85 Marsden et al., 2016). The instrument used by Gemayel et al. (2016) exhibited a maximum ODE of ~2.2% for PSL particle  
86 diameters of 450 nm, while ~1% at 600 nm was the peak ODE reported by Marsden et al. (2016); but only after before the  
87 instrument modification of the instrument. The response of the LAAPTOF to spherical PSL particles smaller than 350 nm and  
88 bigger than 800 nm, and the response to other particle types with different shapes, have not been investigated systematically. The  
89 scattering efficiency (SE), defined as the number percentage-fraction of particles detected by light scattering compared to the  
90 number of particles in the sampled air in front of the aerodynamic inlet lens (ADL) of the instrument (refer to ef-Fig. 1), is  
91 determined by the laser diodes, the detection optics, as well as the photomultiplier tubes (PMT), and has a strong influence on the  
92 ODE of the instrument. Therefore, several groups tried to improve this part of the instrument. Marsden et al. (2016) modified the  
93 detection stage geometry by replacing the detection laser with a fiber coupled 532 nm, 1 W Nd:YAG solid state laser system  
94 with a collimated laser beam, accomplishing an order of magnitude improvement in light detection sensitivity to PSL particles  
95 with 500–800 nm diameter. Zawadowicz et al. (2017) modified the optical path of the laser diodes with a better laser beam of <1  
96 mrad full angle divergence and 100  $\mu$ m detection beam spot size, and applied light guides to enhance the scattered light  
97 collection. This resulted in 2–3 orders of magnitude improvement in optical counting efficiency of incident PSL particles with  
98 500–2000 nm vacuum aerodynamic diameter ( $d_{va}$ ). Zawadowicz et al. (2017) modified the optical path of the laser diodes with a  
99 better laser beam of <1 mrad full angle divergence and 1000  $\mu$ m detection beam spot size, and applied light guides to enhance  
100 the scattered light collection, resulting in 2–3 orders of magnitude improvement in optical counting efficiency to PSL particles  
101 with 500–2000 nm vacuum aerodynamic diameter ( $d_{va}$ ). There are only very few studies so far that discuss mass spectral patterns  
102 of different particle types measured by LAAPTOF. Gemayel et al. (2016) presented spectra from ambient particles collected in  
103 the city centre of Marseille, France; spectra (positive only) from pure soot and SOA coated soot particles were shown by Ahern  
104 et al. (2016); Spectra-spectra from potassium rich feldspar, soot, Argentinian soil dust, and Snomax (commercial ice nuclei)  
105 were shown by Zawadowicz et al. (2017); and PSL and potassium rich feldspar spectra were measured by Marsden et al. (2017);  
106 and radiolytically formed particles spectra were measured by Wonaschuetz et al. (2017). Reitz et al. (2016) presented peak  
107 assignments for pure ammonium nitrate and sulphate particles, as well as for ambient particles measured at a suburban site of  
108 Düsseldorf, Germany, but did not show any spectra. Marker ions generated from SPMS are likely instrument specific, as pointed  
109 out by Schmidt et al. (2017). Therefore, there is a need for publicly available spectral information of this relatively new  
110 instrument.

111 There exists several techniques to group the large number of individual particle types and spectra resulting from SMPS  
112 measurements, such as k-means, c-means, and hierarchical clustering algorithms, neural network based methods such as ART2-  
113 A, as well as the most recent algorithm of ordering points to identify the clustering structure (OPTICS), to help analyse the data  
114 (Hinze et al., 1999; Murphy et al., 2003; Reitz et al., 2016; Zelenyuk et al., 2006b; Zhao et al., 2008). For LAAPTOF data  
115 analysis, the Fuzzy c-means algorithm is commonly used to do classification based on the similarities of the individual spectra.  
116 The number of the classes is chosen manually (Hinze et al., 1999; Reitz et al., 2016). There also exist target (reference

Formatiert: Schriftart: 10 Pt., Nicht Kursiv, Schriftfarbe: Text  
1

Formatiert: Schriftart: 10 Pt., Nicht Kursiv, Schriftfarbe: Text  
1

Feldfunktion geändert

spectra/predefined clusters)-oriented methods that are used for analysing single particle mass spectrometer data, especially for ambient monitoring (Hinz et al., 1999; Gleanta GmbH; LAAPTOF AnalysisPro, Aeromegt GmbH).

In this paper we have characterized our LAAPTOF instrument with respect to its ODE for PSL,  $\text{NH}_4\text{NO}_3$ , and sodium chloride (NaCl) particles for a wide size range ( $d_m$ : 200–2000 nm PSL; 300–1000 nm  $\text{NH}_4\text{NO}_3$  and NaCl). We present laboratory based reference spectra for aerosol particles containing atmospherically relevant major components, which were grouped in three categories: 1) particles consisting of pure compounds, e.g.  $\text{NH}_4\text{NO}_3$ ,  $\text{K}_2\text{SO}_4$ , and organic acids; 2) particles consisting of well-defined mixtures of pure salts and mixtures of organic compounds, e.g.  $\alpha$ -pinene SOA, and PSL internally mixed with  $\text{K}_2\text{SO}_4$ , and as well as other core-shell type of particles; and 3) particles consisting of complex mixtures, e.g. soot and dust particles. These reference spectra may also provide other users comprehensive references for comparison purposes, and thus help better interpretation of ambient data. An example for field data analysis based on reference spectra as well as Fuzzy c-means clustering will be given in chapter 3.3A one-day example of field data interpretation, based on according to the these reference mass spectra based classification as well as the Fuzzy c-means clustering approach, will be given in chapter 3.3 and compared to a Fuzzy clustering approach.

## 2 Methods

### 2.1 The LAAPTOF instrument

The LAAPTOF has been described in several recent publications (Ahern et al., 2016; Gemayel et al., 2016; Marsden et al., 2016, 2017; Reitz et al., 2016; Wonaschuetz et al., 2017; Zawadowicz et al., 2017). Therefore, we only briefly review the general operation steps that yield size and composition information of individual aerosol particles. The LAAPTOF instrument used in this study was delivered in April 2015 and may differ in a few technical aspects from earlier or later versions. A schematic of the main LAAPTOF components is given in Fig. 1 Particles with a vacuum aerodynamic diameter ( $d_{va}$ ) between ~70 nm and 2.5  $\mu\text{m}$  are sampled with a sampling flowrate of ~80 standard cubic centimetre per minute (SCCM), focused and accelerated by an aerodynamic lens, ADL (LPL-2.5, Aeromegt GmbH) with close to 100% transmission efficiency for particles with  $d_{va}$  100 nm to 2  $\mu\text{m}$  ([http://www.aeromegt.com/#products?LPL-2.5\\_details](http://www.aeromegt.com/#products?LPL-2.5_details)), then pass through the particle time-of-flight (PTOF) chamber in which the individual particle can be detected by two sizing laser beams (405 nm continuous wave, 40 mW) separated by 11.3 cm. Based on the particle time of flight between the two laser beams, its  $d_{va}$  can be determined and recorded. After detection by the second sizing laser, a nanosecond (ns) excimer laser pulse (wave length: 193 nm, pulse duration: 4 to 8 ns, maximum pulse energy: ~8 mJ, beam diameter: ~300  $\mu\text{m}$  when it hits the particle (Ramisetty et al., 2017), power density:  $\sim 10^9 \text{ W}\cdot\text{cm}^{-2}$ , ATLEX-S, ATL Lasertechnik GmbH) can be triggered to desorb and ionize particle compounds. A laser pulse energy of 4 mJ was used for all the measurements in this study. More details about the ionization region geometry are given by Ramisetty et al. (2017). The resulting ions are analysed by a bipolar time-of-flight mass spectrometer (BTOF-MS; TOFWERK AG; mass resolution of  $m/\Delta m$  ~600 to 800 at 184 Th, mass range  $m/q=1$  up to ~2000 Th). The resulting cations and anions are detected by corresponding microchannel plate arrays (MCPs), producing a pair of positive and negative spectra for each single particle.

For each type of laboratory generated aerosol particle, we measured at least 300 mass spectra. Data analysis is done via the LAAPTOF Data Analysis Igor software (Version 1.0.2, Aeromegt GmbH). There are five main steps for the basic analysis procedure: a) removal of the excimer laser ringing signal from the raw mass spectra; b) determination of the signal baseline; c) filtering for empty spectra; d) mass calibration; and e) stick integration. Spectra to spectra differences in peak positions due to

Formatiert: Unterstrichen

154 variance in the position of particle-laser interaction complicate the mass calibrations. Details can be found in the supplementary  
155 information (SI). Spectra presented in this paper were typically normalized to the sum of ion signal before further aggregation.

156 For the grouping of ambient data, we used two different classification methods. The Fuzzy c-means clustering algorithm is  
157 embedded in the LAAPTOF Data Analysis Igor software and starts from random class centres. Particle spectra with a minimum  
158 distance between their data vectors and a cluster centre will be grouped into this specific class (Hinz et al., 1999). Since each  
159 spectrum can belong to multiple classes (Reitz et al., 2016) the resulting fraction/percentage for each class represents the  
160 information about the degree of similarity between aerosol particles in one particular class, and not a number percentage. The  
161 second method developed in this study is based on the correlation between each ambient spectrum and our reference spectra. The  
162 resulting Pearson's correlation coefficient ( $r$ ) is used as the criteria to group particles into different types (here we use "types"  
163 instead of "classes" in order to differentiate these two classification methods). When  $r$  is above the threshold value 0.6, the  
164 ambient spectrum is considered to have high correlation with the corresponding reference spectra. For simplification we chose 10  
165 positive and 7 negative reference spectra. For example, we only use German soil dust as the reference for arable soil dust rather  
166 than using four arable soil dust samples from different places. More details about the procedure for this method as well as the  
167 corresponding equations and uncertainties estimation can be found in the supplementary information.

## 168 2.2 Aerosol particle generation and experimental set up in the laboratory

169 The laboratory based aerosol particles measured in this study (summarized in Table 1) were generated in four different ways (A,  
170 B1, B2, and S).

171 Method A: Samples for pure particles and homogeneous and heterogeneous mixtures were dissolved/suspended in purified  
172 water and nebulized (ATM 221; Topas GmbH) with dry synthetic air, passed through two diffusion dryers (cylinder filled with  
173 Silica gel, Topas GmbH), and then size selected by a Differential Mobility Analyser (DMA 3080, TSI GmbH) before being  
174 sampled by LAAPTOF.

175 Method B1: Particles were sampled from the 84.5 m<sup>3</sup> simulation chamber AIDA (Aerosol Interactions and Dynamics in the  
176 Atmosphere) of KIT (Saathoff et al., 2003). SOA particles were formed in the 3.7 m<sup>3</sup> stainless steel Aerosol Preparation and  
177 Characterization (APC) chamber via ozonolysis (~6 ppm ozone) of  $\alpha$ -pinene (~2.2 ppm) and then transferred into AIDA. Soil  
178 dust samples were dispersed by a rotating brush generator (RGB1000, PALAS) and injected via cyclones into the AIDA  
179 chamber. Sea salt particles were generated and injected into AIDA by ultrasonically nebulizing artificial seawater (Sigma Aldrich)  
180 and highly concentrated skeletonema marinoi culture (in artificial seawater), respectively, via a droplet separator and 2 diffusion  
181 dryers (Wagner et al., 2017).

182 Method B2: Used only for soot particles, which were generated with a propane burner (RSG miniCAST; Jing Ltd.) and  
183 injected into and sampled from a stainless steel cylinder of 0.2 m<sup>3</sup> volume.

184 Method S: Silica, Hematite, Illite NX, Arizona test dust, desert and urban dust, black carbon from Chestnut wood  
185 (University of Zürich, Switzerland), and diesel soot reference particles from NIST were suspended in their reservoir bottles by  
186 shaking them and sampled directly from the headspace (upper part) of these reservoirs through a tube connecting it with the  
187 LAAPTOF.

188 For all the measurements, except measuring the method S-generated particles, a condensation particle counter (CPC 3010, TSI  
189 GmbH) was used to record the particle number concentration in parallel with the LAAPTOF inlet. Setup in Fig. 1 was specific  
190 for particles generated from method A. The laboratory based aerosol particles measured in this study (summarized in  
191 Table S1/ Table 1) were generated in three four different ways (cf. Fig. 1 A, B1, B2, and S). Method A, S samples for pure particles  
192 (except SiO<sub>2</sub>) and homogeneous and heterogeneous mixtures (except SOA) were dissolved/suspended in purified water and

Formatiert: Schriftart: Nicht Kursiv, Schriftfarbe: Text 1

Formatiert: Block, Abstand Nach: 0 Pt., Zeilenabstand: 1,5  
Zeilen

Formatiert: Schriftart: Nicht Kursiv, Schriftfarbe: Text 1

Formatiert: Schriftart: Nicht Kursiv, Schriftfarbe: Text 1

193 nebulized (ATM 221; Topas-GmbH) with dry synthetic air, passed through two diffusion dryers (cylinder filled with Silica-gel,  
194 Topas-GmbH), and then size selected by a Differential Mobility Analyser (DMA 3080, TSI GmbH) before being sampled by  
195 LAAPTOF. Method B1, the particles finally formed in the 84.5 m<sup>3</sup> simulation chamber AIDA (Aerosol Interactions and  
196 Dynamics in the Atmosphere) of KIT (Saathoff et al., 2003). (setup A). A condensation particles counter (CPC 3010, TSI GmbH)  
197 was used to record the particle number concentration. SOA particles from ozonolysis (~6 ppm ozone) of  $\alpha$  pinene (~2.2 ppm), a  
198 common laboratory based surrogate for biogenic SOA (Saathoff et al., 2009), were formed in the 3.7 m<sup>3</sup> stainless steel Aerosol  
199 Preparation and Characterization (APC) chamber and then transferred into the AIDA chamber the 84.5 m<sup>3</sup> simulation chamber  
200 AIDA (Aerosol Interactions and Dynamics in the Atmosphere) of KIT (Saathoff et al., 2003). Soil dust samples were dispersed  
201 by a rotating brush generator (RGB1000, PALAS) and injected via cyclones into the AIDA chamber. Sea salt particles were  
202 generated in different ways Pure and the organics containing sea salt particles were generated and injected into AIDA by adding  
203 the ultrasonically nebulizing artificial seawater (Sigma Aldrich) and highly concentrated skeletonema marinoi culture (in artificial  
204 seawater) ultrasonically nebulized, respectively, via a droplet separator and 2 diffusion dryers (Wagner et al., 2017) and sampled  
205 from the AIDA chamber (setup B in Fig. 1). Method B2 is used only for S<sub>500</sub> particles, which were from incomplete  
206 combustion of propane were generated with a propane burner (RSG miniCAST; Jing Ltd.) and injected into and sampled from a  
207 stainless steel cylinder of 0.2 m<sup>3</sup> volume. Method S corresponds to particles mobilized by shaking in a reservoir, which was used  
208 for silica, Hematite, Illite\_NX, Arizona test dust, desert and urban dust, black carbon from Chestnut wood (University of Zürich,  
209 Switzerland), and diesel soot reference particles from NIST were sampled directly from a reservoir (e.g. bottle) through a tube  
210 connecting it with the LAAPTOF after having been suspended by shaking the reservoir (Method S). S were mobilized in their  
211 reservoir bottles by shaking and sampled directly from the headspace (upper part) of these reservoirs through a tube connecting it  
212 with the LAAPTOF (Method S).

213 Ambient aerosol particles from a rural site near Leopoldshafen, Germany (refer to section 2.3) were sampled through a PM<sub>2.5</sub>  
214 inlet (SH 2.5-16, Comde-Derenda GmbH) with 1 m<sup>3</sup> h<sup>-1</sup>, a fraction of which was guided into the LAAPTOF (set up C in Fig. 1).  
215 Silica, Hematite, Illite\_NX, mineral dust, black carbon from Chestnut wood (University of Zürich, Switzerland), and urban dust  
216 and diesel soot reference particles from NIST, were directly sampled from the headspace of their reservoirs. The aforementioned  
217 particles were then sampled and measured by LAAPTOF. Method S generated particles in the headspace (upper part) of their  
218 reservoirs were directly sampled through a tube connected with the instrument inlet before their sedimentation to the bottom. For  
219 the other measurements, a condensation particles counter (CPC 3010, TSI GmbH) was used to record the particle number  
220 concentration in front of the LAAPTOF inlet. TABE in Fig. 1 was specific for particles generated from method A.  
221 (setup A). A condensation particles counter (CPC 3010, TSI GmbH) was used to record the particle number concentration.

### 222 2.3 Field measurement

223 Unusually high particle number concentrations, similar to downtown Karlsruhe (a city in southwest Germany), were observed  
224 frequently northeast of Karlsruhe by particle counters on-board a tram wagon (www.aero-tram.kit.edu) intersecting the city  
225 (Hagemann et al., 2014). To study the nature and to identify possible sources of these particles, their number, size, chemical  
226 composition, associated trace gases, and meteorological conditions were measured from July 15<sup>th</sup> to September 1<sup>st</sup>, 2016 at a  
227 rural location (49°6'10.54"N, 8°24'26.07"E), next to the tram line north of the village of Leopoldshafen, Germany. Ambient  
228 aerosol particles were sampled through a PM<sub>2.5</sub> inlet (SH 2.5 - 16, Comde-Derenda GmbH) with 1 m<sup>3</sup> h<sup>-1</sup>, a fraction of which was  
229 guided into the LAAPTOF, which was deployed for ~5 weeks from July 26 to August 31. LAAPTOF measurements provided  
230 information on size and mass spectral patterns for individual particles. In this paper we use data from one day as an example for  
231 the potential interpretation of LAAPTOF spectral data using reference spectra.

## 2.4 Efficiency calculations

In the literature there are two definitions of detection efficiency (DE) of SPMS used: one is equal to the scattering efficiency (SE) of the detection lasers (Brands et al., 2011; Gaie-Levrel et al., 2012; Su et al., 2004; Zelenyuk and Imre, 2005; Zelenyuk et al., 2009), which is the fraction of particles detected by the scattering optics in the detection region of the instrument; the other one is the product of SE and hit rate (HR) of the ablation/ionization laser (Su et al., 2004; Gemayel et al., 2016; Marsden et al., 2016). The hit rate is the fraction of particles detected leading actually to a useful mass spectrum. In this paper we use overall detection efficiency (ODE), defined by the following equations:

$$ODE = SE \times HR \times 100\% \quad (1)$$

$$SE = N_d/N_0 \times 100\% \text{ (transmission efficiency of ADL is included)} \quad (2)$$

$$HR = N_p/N_d \times 100\% \text{ (ionization efficiency is included)} \quad (3)$$

$$N_0 = C_0 \times \text{flowrate} \times \text{time} \quad (4)$$

where  $N_d$  is the number of particles detected by light scattering,  $N_0$  is the number of particles in front of the ADL,  $N_p$  the number of bipolar spectra,  $C_0$  is the particle number concentration ( $\text{cm}^{-3}$ ) measured by a CPC in front of the ADL and the flowrate is the LAAPTOF sample flowrate.

## 2.5 Spectral and size data analysis

For each type of laboratory generated aerosol particle, we measured at least 300 mass spectra. Data analysis is done via the LAAPTOF Data Analysis Igor software (Version 1.0.2, Aeromegt GmbH). There are five main steps for the basic analysis procedure: a) removal of the excimer laser ringing signal from the raw mass spectra; b) determination of the signal baseline; c) filtering for empty spectra; d) mass calibration; and e) stick integration, that is the integration of nominal masses for peaks. It should be noted that spectrum-to-spectrum differences in peak positions for the same ion fragments/clusters complicate the mass calibrations. This may be caused by differences in kinetic energy of the ions produced, however this effect is typically compensated in the TOFs with reflectron (Kulkarni et al., 2011). Spectrum-to-spectrum peak shifts, especially in the positive spectra in our study, are mainly because of variance in the position of particle-laser interaction, which cannot be corrected with the existing Aeromegt software or the LAAPTOF instrument (Ramisetty et al., 2017). Details can be found in 'Procedure 1' in the supplementary information (Kulkarni et al., 2014). Spectra presented in this paper were typically normalized to the sum of ion signal before further aggregation.

For ambient data analysis, we used two different classification methods. The first one is Fuzzy c-means clustering algorithm embedded in the LAAPTOF Data Analysis Igor software, commonly used to do classification based on the similarities of the individual spectra. The number of the classes is chosen manually, afterwards the particle spectra with a minimum distance between their data vectors and a cluster centre will be grouped into a specific class (Hinz et al., 1999; Reitz et al., 2016). Since each spectrum can belong to multiple classes (Reitz et al., 2016) the resulting fraction/percentage for each class represents the information about the degree of similarity between aerosol particles in one particular class, and not a number percentage. The second method developed in this study is based on the correlation between each ambient spectrum and our reference spectra. The resulting Pearson's correlation coefficient ( $r$ ) is used as the criterion to group particles into different types (here we use "types" instead of "classes" in order to differentiate these two classification methods). When  $r$  is higher than a threshold value of 0.6, the ambient spectrum is considered to have high correlation with the corresponding reference spectrum. The resulting Pearson's correlation coefficient ( $r$ ) is used as the criteria to group particles into different types (here we use "types" instead of "classes" in order to differentiate these two classification methods). When  $r$  is above the threshold value 0.6, the ambient spectrum is

Formatiert: Keine, Abstand Vor: 0 Pt., Nach: 0 Pt.,  
Zeilenabstand: 1,5 Zeilen

Formatiert: Schriftart: Nicht Kursiv, Schriftfarbe: Text 1

266 ~~considered to have high correlation with the corresponding reference spectra.~~ For simplification we chose 10 positive and 7  
267 ~~negative reference spectra.~~ For example, we only use German soil dust as the reference for arable soil dust rather than using four  
268 ~~arable soil dust samples from different places.~~ More details about the procedure for this method as well as the corresponding  
269 ~~equations and uncertainties estimation can be found in “Procedure 2” in the supplementary information.~~

270 ~~In addition, particle size ( $d_{va}$ ) was recorded for individual particles. The corresponding size distribution can be plotted as  $d_{va}$~~   
271 ~~histogram, a Gaussian fit of which yields number mean  $d_{va}$  values and the standard deviation (width).~~~~In addition, particle size~~  
272 ~~( $d_{va}$ ) was recorded for individual particles and the corresponding size distribution can be shown from the  $d_{va}$  histogram, which~~  
273 ~~also provides the expected  $d_{va}$  values and the standard deviation (width) from Gaussian fitting.~~

Formatiert: Schriftart: Nicht Kursiv, Schriftfarbe: Text 1

## 274 3 Results and Discussion

### 275 3.1 Determination of LAAPTOF performance parameters

#### 276 3.1.1 Hit rate, Scattering efficiency, hit rate and overall detection efficiency for standard samples

277 In the literature there are two definitions of detection efficiency (DE) of SPMS used: one is equal to the scattering efficiency (SE)  
278 of the detection lasers (Brands et al., 2011; Gaie-Levrel et al., 2012; Su et al., 2004; Zelenyuk and Imre, 2005; Zelenyuk et al.,  
279 2009), while the other one is the product of SE and hit rate (HR) of the ablation/ionization laser (Su et al., 2004; Gemayel et al.,  
280 2016; Marsden et al., 2016). The hit rate (HR) is the fraction of particles detected by the scattering optics leading actually to a  
281 useful mass spectrum. In this paper we use overall detection efficiency (ODE), defined by the following equations:

$$282 \text{ODE} = \text{SE} \times \text{HR} \times 100\% \quad (1)$$

$$283 \text{SE} = N_d/N_0 \times 100\% \text{ (transmission efficiency of ADL is included)} \quad (2)$$

$$284 \text{HR} = N_d/N_a \times 100\% \text{ (ionization efficiency is included)} \quad (3)$$

$$285 N_0 = C_a \times \text{flowrate} \times \text{time} \quad (4)$$

286 Hit rate (where  $N_d$  is the number of particles detected by light scattering,  $N_0$  is the number of particles in front of the ADL,  $N_a$  the  
287 number of bipolar spectra, and  $C_a$  is the particle number concentration ( $\text{cm}^{-3}$ ) measured by a CPC in front of the ADL. The  
288 sample flowrate of the LAAPTOF is  $\sim 80 \text{ cm}^3 \text{ min}^{-1}$ .

289 HR), scattering efficiency (SE), and overall detection efficiency (ODE) for spherical PSL particles as a function of electrical  
290 mobility equivalent diameter  $d_m$ , are plotted in Fig. 2. It should be noted that the LAAPTOF detection behaviour may vary  
291 depending on the alignment of the ADL and the optical components (especially the detection laser diodes), which is difficult to  
292 reproduce. We therefore show results for PSL particles based on 2 repeated experiments after 3 alignments each, and thus a total  
293 of 6 experiments for each data point. The uncertainty intervals in Fig. 2 are the difference between the maximum/minimum and  
294 the average values obtained from these 6 experiments. As shown in panel A of Fig. 2, for particle diameters from 200 to 400 nm,  
295  $\text{HR}_{\text{PSL}}$  exhibits an increase from 69% to 94%, decreases to 83% for 700 nm particles, and then becomes stable at  $\sim 85\%$  for  
296 particles with diameters up to 2  $\mu\text{m}$ . The average  $\text{HR}_{\text{PSL}}$  ( $\overline{\text{HR}}_{\text{PSL}}$ ) is  $\sim 84\%$ .  $\text{SE}_{\text{PSL}}$  and  $\text{ODE}_{\text{PSL}}$  show an M-like shape with two  
297 peaks, at 500 nm ( $\text{SE}_{\text{PSL}}$  3.0%,  $\text{ODE}_{\text{PSL}}$  2.7%), and at 1000 nm ( $\text{SE}_{\text{PSL}}$  4.8%,  $\text{ODE}_{\text{PSL}}$  4.2) (see panel B and C of Fig. 2). We  
attribute this behaviour to a combined effect of the spherical shape of PSL particles and the optical system of this instrument, e.g.  
Mie resonances related to particle size and laser wavelength (see section 3.1.2 for details). As shown in panel C of Fig. 2, values  
and trends of  $\text{ODE}_{\text{PSL}}$  in the size range of 300–800 nm of our instrument are similar to those reported by Gemayel et al. (2016)  
and Marsden et al. (2016) –for their LAAPTOF instruments. A recent LAAPTOF study by Zawadowicz et al. (2017) shows

Formatiert: Einzug: Erste Zeile: 0 cm

298 comparable results for PSL particles with  $d_p \leq 500$  nm, and an M-like shape of ODE in the size range of 200–2000 nm (after  
299 instrument modification).

300 We also measured mass spectra of non-spherical  $\text{NH}_4\text{NO}_3$  ( $\chi=0.8$ , Williams et al., 2013) and NaCl particles (cubic,  $\chi=1.06$  to  
301 1.17, Zelenyuk et al., 2006a). Similar as for PSL particles,  $\text{NH}_4\text{NO}_3$ , and NaCl particles show relatively high and stable HR with  
302 average values of 80% and 66% (see panel D in Fig. 2), thus SE and ODE have a similar trend. No M-like shape of ODE as a  
303 function of particle size is observed due to the different light scattering properties of the non-spherical salt particles (Bohren and  
304 Huffman, 2007) (see panels E and F in Fig. 2). Comparable results were shown for  $(\text{NH}_4)_2\text{SO}_4$  particles ( $\chi=1.03$  to 1.07,  
305 Zelenyuk et al., 2006a) by Zawadowicz et al. (2017). As shown in Fig. 2 E–F, SE and ODE decrease with increasing shape factor  
306 for salt particles of the same size. We will discuss this in more detail in the following section.

### 307 3.1.2 Factors influencing overall detection efficiency

308 There are various factors that can influence the ODE of LAAPTOF. One of these is particle size. For particles with diameters  
309 below 200 nm, the scattered light becomes too weak to be detected due to the strong dependence of the scattering intensity on  
310 particle size (Bohren and Huffman, 2007). For particles with diameters larger than 2  $\mu\text{m}$ , focusing by the ADL is much less  
311 efficient, resulting in a higher divergence of the particle beam (Schreiner et al., 1999). This lowers the probability of larger  
312 particles to be detected by the detection/scattering laser and/or to be hit by the ionization laser. In addition, light scattering of  
313 spherical particles like PSL changes from Rayleigh to Mie to Geometric scattering as the size parameter  $\alpha=\pi d_p/\lambda$  increases from  
314  $\ll 1$  to  $\sim 1$  to  $\gg 1$  (Seinfeld and Pandis, 2006). The scattering efficiencies of PSL particles, based on Mie calculation at the  
315 particle sizes and detection laser wavelength relevant to our LAAPTOF measurement, validate the  $\alpha$ -ranges from 1.5 to 19 for  
316 200–2500 nm PSL particles, and is thus in the Mie-scattering regime and the reason for the M-like shape of  $\text{SE}_{\text{PSL}}$  (refer to Fig.  
317 S1) and  $\text{ODE}_{\text{PSL}}$ . As long as the particle diameter ( $d_p$ ) is smaller than the wavelength of the detection laser light, here 405 nm, the  
318 scattered radiation intensity (proportional to  $d_p^6$ ) will rapidly decrease with decreasing particle sizes, resulting in low ODE. ODE  
319 is e.g. 0.01% for 200 nm PSL particles. For non-spherical particles like salts, their SE and ODE are also size dependent (panel F  
320 in Fig. 2), due to size-dependent light scattering ability and particle beam divergence. However, in the size range of 300 to 1000  
321 nm studied here, they don't exhibit Mie resonance, and thus don't show an M-like shape in their scattering efficiency.

322 Optical properties of the particles have a strong impact on how light is scattered and absorbed, and thus it should be noted  
323 that the optical properties do not only influence scattering efficiency, but also absorption and ionization efficiency (or hit rate).  
324 As shown in Fig. 2F, ODE for  $\text{NH}_4\text{NO}_3$  is higher than that for NaCl at any size we studied. This is mainly caused by differences  
325 in their optical properties of scattering. Relative fresh soot particles scatter only little light due to their black colour and small  
326 size (typically  $\sim 20$  nm) of the primary particles forming their agglomerates, and are thus hardly detected by the detection laser.  
327 However they are good light absorbers and thus relatively easy to ablate and ionize. The reference spectra of pure  $\text{NH}_4\text{NO}_3$  and  
328  $(\text{NH}_4)_2\text{SO}_4$  particles showed intensive prominent peaks for pure  $\text{NH}_4\text{NO}_3$  particles (refer to Fig. 3A) but only one weak peak of  
329  $m/z$  30  $\text{NO}^+$  for pure  $(\text{NH}_4)_2\text{SO}_4$  particles. This indicates that  $\text{NH}_4\text{NO}_3$  is a better absorber than  $(\text{NH}_4)_2\text{SO}_4$ , and thus easier to  
330 ablate and ionize. For homogeneous mixtures of these two ammonium salts, the sulphate species are ablated and ionized much  
331 more easily (refer to section 3.2.2), due to increased UV light absorption by the nitrate component. Some small organic  
332 compounds with weak absorption properties are hard to ablate and ionize, e.g. oxalic acid ( $\text{C}_2\text{H}_2\text{O}_4$ ), pinic acid, and cis-pinonic  
333 acid. They exhibited much weaker signals ( $\sim 80\%$  lower) than macromolecular organic compounds in PSL or humic acid  
334 particles.

335 Optical properties of the particles have a strong impact on how light is scattered and absorbed, and thus also greatly influence  
336 scattering efficiency and ionization efficiency (or hit rate), respectively. As shown in Fig. 2, ODE for  $\text{NH}_4\text{NO}_3$  is higher than that

Feldfunktion geändert

Feldfunktion geändert

Formatiert: Nicht Hervorheben

Formatiert: Schriftart: Nicht Kursiv, Schriftfarbe: Text 1

Formatiert: Schriftart: Nicht Kursiv, Schriftfarbe: Text 1

for NaCl at any size we studied (panel F). This is caused by differences in their optical properties and shapes. Soot particles are good light absorbers and thus relatively easy to ablate and ionize. However they scatter only little light due to the small size (typically ~20 nm) of the primary particles forming their agglomerates, and are thus hardly detected. Their usually small size is an additional disadvantage for their detection.

acid. The reference spectra of pure  $\text{NH}_4\text{NO}_3$  and  $(\text{NH}_4)_2\text{SO}_4$  particles showed intensive prominent peaks for pure  $\text{NH}_4\text{NO}_3$  particles but only one weak peak for pure  $(\text{NH}_4)_2\text{SO}_4$  particles. This is indicating that  $\text{NH}_4\text{NO}_3$  is a better absorber than  $(\text{NH}_4)_2\text{SO}_4$ , and thus easier to ablate and ionize. For homogeneous mixtures of these two ammonium salts, the sulphate species are detected much more easily due to increased light absorption by the nitrate component (refer to section 3.2.2). Soot particles are good light absorbers and thus relatively easy to ablate and ionize. However they scatter only little light due to the small size (typically ~20 nm) of the primary particles forming their agglomerates, and are thus hardly detected. Their usually small size is an additional disadvantage for their detection. Some small organic compounds with weak absorption properties are hard to ablate and ionize as well, e.g. oxalic acid ( $\text{C}_2\text{H}_2\text{O}_4$ ), pinic and cis-pinonic acids measured in this study had much weaker signals in the spectra (~80% lower) than macromolecular organic compounds in PSL or humic acid particles.

Particle morphology is another important factor. The scattering efficiency for non-spherical  $\text{NH}_4\text{NO}_3$  is higher than for spherical PSL particles in the size range of 300–800 nm (Fig. 2 B–E) (Ackerman et al., 2015). For larger particle sizes ( $d_m > 800$  nm), beam divergence offsets the shape effect (Murphy, 2007). Apart from that, the increase of surface roughness and inhomogeneity can promote the scattering capability of particles (Ackerman et al., 2015).

The incident intensity of radiation, which is another parameter that influences the light scattered by particles (as well as background signal caused by stray light), is related to power and beam dimensions of the detection laser. Corresponding instrument modifications were done. The incident intensity of radiation, which is another parameter that influences the light scattered by particles (as well as background signal caused by stray light), is related to power and beam dimensions of the detection laser. Corresponding instrument modifications were done by Marsden et al. (2016) and Zawadowicz et al. (2017) (refer to section 1). In addition, alignment of the excimer laser focus in x, y, and z position influences optimum hit rates (Ramisetty et al., 2017). The incident intensity of radiation, which is another parameter that influences the light scattered by particles (as well as background signal caused by stray light), is related to power and beam dimensions of the laser. A laser power of 40 mW was used in this study. Marsden et al. (2016) replaced the detection laser with a fibre coupled 532 nm, 1 W Nd:YAG solid state laser system that has a collimated laser beam, resulting in an order of magnitude improved sensitivity to PSL particles with 500–800 nm diameter. Zawadowicz et al. (2017) used laser diodes with a laser beam of <1 mrad full angle divergence and 1000  $\mu\text{m}$  detection beam spot size, and applied light guides to enhance the scattered light collection, resulting in 2–3 orders of magnitude improvement in optical counting efficiency of PSL particles with  $d_{va}$  500–2000 nm. In addition, alignment of the excimer laser focus in x, y, and z position influences optimum hit rates (Ramisetty et al., 2017).

There are further instrumental aspects that affect the detection efficiency. High number concentrations of the incoming particles influence the ODE, since there can be more than one particle present between the two detection lasers. The transmission efficiency of the ADL is included in the scattering efficiency, and thus directly influences it. The size range of particles focused in the lens, and the particle beam width strongly depend on the configuration of the ADL (Canagaratna et al., 2007; Johnston, 2000). Liu lenses and Schreiner lenses can focus the particles in the size range of 80–800 nm, and 300–3000 nm, respectively (Kamphus et al., 2008; Liu et al., 1995; Schreiner et al., 1999). The ADL transmission efficiency of our instrument, as determined by the manufacturer (Aeromegt GmbH), is close to 100% for particles with  $d_{va}$  100–2000 nm.

### 3.2 LAAPTOF reference spectra of laboratory generated particle types

Formatiert: Schriftart: (Standard) Times New Roman, 10 Pt.,  
Schriftfarbe: Text 1

Formatiert: Schriftart: Nicht Kursiv, Schriftfarbe: Text 1

Feldfunktion geändert

Feldfunktion geändert

Feldfunktion geändert

Feldfunktion geändert

Formatiert: Schriftart: (Standard) Times New Roman, 10 Pt.,  
Schriftfarbe: Text 1

376 Particles for which reference spectra are presented here are listed in [Table S4Table 1](#). For each type of these aerosol particles, we  
377 present averaged spectra for typically 300 to 500 single particles. The relative standard deviations (RSD, SD normalized to signal)  
378 for the characteristic peaks are in the range of 15–186%, median value 77%.

379 Despite the lack of full quantitiveness of the LAAPTOF, mass spectral signal amplitudes show an increase with particle  
380 size (refer to [Fig. S2](#)). However, no systematic changes in the mass spectral signatures were observed for different particle sizes.  
381 Therefore, [for the samples passing through the DMA](#), particles in the optimum size range of the LAAPTOF ( $d_m = 800$  nm) and  
382 with good signal-to-noise ratio were chosen to generate reference spectra. For polydisperse particles generated in the AIDA  
383 chamber, the corresponding average spectra include particles of broader size distributions compared to those preselected by the  
384 DMA. Information on particle generation or source as well as the sizes is listed in [Table S4Table 1](#).

385 A qualitative comparison between the relative peak intensity ratios within an single particle spectrum and those in another  
386 spectrum can yield relative quantitation information, as suggested by Gross et al. (2000). We add information on typical peak  
387 ratios to some of our reference spectra to help identify specific species.

### 388 3.2.1 Pure compound particles

389 Although particles consisting of one single species only are rarely sampled in the atmosphere, interpretation of mass spectra of  
390 ambient samples is supported by the knowledge about the mass spectra of pure compounds. In the following mass spectra for a  
391 few typical ambient aerosol constituents are discussed.

392 Figure 3 shows average spectra for pure compound aerosol particles. For  $\text{NH}_4\text{NO}_3$  particles (panel A), we observed the  
393 positive ions  $m/z$  18  $\text{NH}_4^+$  and  $m/z$  30  $\text{NO}^+$ ; and the negative ions  $m/z$  46  $\text{NO}_2^-$  and  $m/z$  62  $\text{NO}_3^-$ , similar to Reitz et al. (2016).  
394 The LAAPTOF is much less sensitive to ammonium than nitrate fragments, leading to a weak  $\text{NH}_4^+$  signal and prominent  $\text{NO}^+$ ,  
395  $\text{NO}_2^-$  and  $\text{NO}_3^-$  peaks. The ratio of  $\text{NO}^+$  to  $\text{NH}_4^+$  is  $\sim 48$ , and the ratio of  $\text{NO}_2^-$  to  $\text{NO}_3^-$  is  $\sim 4$ . The prominent peak of  $\text{NO}^+$  arises not  
396 only from nitrate (majority), but also from ammonium (Murphy et al., 2006). In our ammonium nitrate spectra, there are weaker  
397 signatures of  $m/z$  46  $\text{NO}_2^-$  and  $m/z$  125  $\text{HNO}_3\text{NO}_3^-$  (not shown here, but visible and reproducible), which were also observed in  
398 PALMS mass spectra (Zawadowicz et al., 2015). For  $\text{K}_2\text{SO}_4$  particles, we observed the potassium signals at  $m/z$  39  $\text{K}^+$  and  $m/z$   
399 41  $\text{K}^+$ , and a sulphate signature with ion clusters grouped around  $m/z$  32  $\text{S}^-$ ,  $m/z$  64  $\text{SO}_2^-$ ,  $m/z$  80  $\text{SO}_3^-$  and  $m/z$  96  $\text{SO}_4^-$ . [Note that](#)  
400 [the extra peak at  \$m/z\$  40<sup>+</sup> besides  \$m/z\$  39  \$\text{K}^+\$  in Fig. 3 \(B\) is likely due to the incorrect mass assignments as a result of peak shifts](#)  
401 [\(refer to section 2.5 and “Procedure 1” in the supplementary information\). For high-intensity peaks such as sodium chloride](#)  
402 [NaCl, extra peaks next to the main peak \(Fig. S23\) may have an additional reason: “ringing” due to partial saturation of the data](#)  
403 [acquisition system or signal reflections within the data acquisition circuitry \(Gross et al., 2000\). Note that the extra peak at  \$m/z\$](#)   
404 [40<sup>+</sup> besides  \$m/z\$  39  \$\text{K}^+\$  in Fig. 3 \(B\) is likely due to the incorrect mass assignments for the some stick spectra as a result of peak](#)  
405 [shifts \(refer to section 2.5 and “Procedure 1” in supplementary information\). For other cases such as sodium chloride NaCl, there](#)  
406 [is an extra peak at  \$m/z\$  36<sup>-</sup> besides the main one at  \$m/z\$  35  \$\text{Cl}^-\$  \(Fig. S2\). This is most likely because of that the peaks with high](#)  
407 [intensity may exhibit some “ringing”, resulting in multiple peaks for a particular ion in a mass spectrum, peaks with high](#)  
408 [intensity exhibit “ringing” in the raw spectra, resulting in small peaks beside the main ones in the integrated stick spectra \(Gross](#)  
409 [et al., 2000\), such as  \$m/z\$  40<sup>+</sup> besides  \$m/z\$  39  \$\text{K}^+\$  in Fig. 3 \(B\), and  \$m/z\$  36<sup>-</sup> besides  \$m/z\$  35  \$\text{Cl}^-\$  in the spectra for sodium chloride](#)  
410 [NaCl \(Fig. S1\). Therefore, the real intensities of  \$m/z\$  39  \$\text{K}^+\$  and of  \$m/z\$  35  \$\text{Cl}^-\$  should include their-its corresponding side ringing](#)  
411 [peaks. For](#) The ratio of  $m/z$  39  $\text{K}^+$  to  $m/z$  41  $\text{K}^+$  is  $\sim 13.2$ , close to the natural isotopic ratio of  $\sim 13.9$  for  $^{39}\text{K}/^{41}\text{K}$ . For pure NaCl  
412 particles, the ratio of  $m/z$  35  $\text{Cl}^-$  to  $m/z$  37  $\text{Cl}^-$  is  $\sim 3.2$ , similar to the natural isotopic ratio of  $\sim 3.1$  for  $^{35}\text{Cl}/^{37}\text{Cl}$ . Therefore, these  
413 two isotopic ratios can be used as markers to identify K and Cl measured by LAAPTOF. Another inorganic compound measured

Formatiert: Standard, Leerraum zwischen asiatischem und westlichem Text nicht anpassen, Leerraum zwischen asiatischem Text und Zahlen nicht anpassen

Formatiert: Schriftart: Nicht Kursiv, Schriftfarbe: Text 1

Formatiert: Schriftart: Nicht Kursiv, Schriftfarbe: Text 1

Formatiert: Schriftart: Nicht Kursiv, Schriftfarbe: Text 1

Feldfunktion geändert

Feldfunktion geändert

here is silica (Fig. S2Fig. S4) and its with the typical peak ratio of  $(m/z\ 76\ \text{SiO}_3^- + m/z\ 77\ \text{HSiO}_3^-)$  to  $m/z\ 60\ \text{SiO}_2^-$  is  $\sim 1.0$ . The corresponding histograms of such ratios for different particle samples can be found in Fig. S3Fig. S5.

High signal intensities in oxalic acid spectra are observed at  $m/z\ 18\ \text{H}_2\text{O}^+$ ,  $28\ \text{CO}^+$ , and  $30\ \text{CH}_2\text{O}^+$ , as well as some weaker peaks at  $m/z\ 40^+$ ,  $44^+$ ,  $56^+$ , and  $57^+$ .  $M/z\ 89\ \text{C}_2\text{O}_4\text{H}^-$  is used as signature ion for oxalic acid in other SPMS studies (Roth et al., 2016). In our study, a distinct signal at around  $m/z\ 89^-$  is observed as well, indicating oxalate fragment formation after laser ablation.

In order to identify humic like substances in the ambient particles, we measured humic acid particles (Fig. S4Fig. S6) and found hydrocarbon and elemental carbon fragments, with very prominent peaks at  $m/z\ 24^-$ ,  $25^-$ , and  $26^-$  suggested to be organic ions (Silva et al., 2000), as well as peaks at  $m/z\ 25^-$ ,  $26^-$ ,  $49^-$ , and  $73^-$  for unsaturated organic compounds.

### 3.2.2 Particles consisting of well-defined internal mixtures

Figure 4 shows average spectra from homogeneously internally mixed particles. The spectrum from the mixture of  $\text{NH}_4\text{NO}_3$  and  $(\text{NH}_4)_2\text{SO}_4$  (panel A) contains the signature from pure  $\text{NH}_4\text{NO}_3$  particles, but with lower relative intensities (each peak intensity is normalized to the sum of ion signal) for  $\text{NO}_2^-$  and  $\text{NO}_3^-$ , due to the formation of anion clusters at  $\sim m/z=80\ \text{SO}_3^-$  and  $97\ \text{HSO}_4^-$ . In addition, compared to the pure  $\text{NH}_4\text{NO}_3$  particles, the ratio of  $\text{NO}^+$  to  $\text{NH}_4^+$  ( $\sim 34$ ) is  $\sim 30\%$  lower in the spectrum for the mixture, due to its lower molar ratio of nitrate/ammonium, whereas the ratio of  $\text{NO}_2^-$  to  $\text{NO}_3^-$  ( $\sim 7$ ) is  $80\%$  higher. In addition, as already discussed in section 3.1.2, the better UV light absorber  $\text{NH}_4\text{NO}_3$  Nitrate is believed to assist in light absorbing for the mixed particles, resulting in a sulphate signature that could not be observed for pure  $(\text{NH}_4)_2\text{SO}_4$ . This exemplifies potential effects of individual particle chemical composition on mass spectral performance of the LAAPTOF. For the mixture of  $\text{K}_2\text{SO}_4$  and NaCl (panel B), similar signatures as for the pure particles were observed. Compared to the pure NaCl particle spectra, the signal intensity of  $\text{Na}^+$  is decreased. This can be explained by more cations formed from the mixed particles, including from potassium, which has a higher ionization potential and lower lattice energy than NaCl. For the mixed particles, expected clusters such as  $113/115\ \text{K}_2\text{Cl}^+$ ,  $109\ \text{KCl}_2^+$ , and  $119\ \text{NaSO}_4^+$  and a minor fragment  $97\ \text{KNaCl}^+$  were observed, but not  $81/83\ \text{Na}_2\text{Cl}^+$  as found in pure NaCl particles. These results show that compared to pure compounds, mass spectra from aerosol particles consisting of mixtures can feature new ions, while some marker ions for the pure compounds may disappear. These spectra are thus not simply a combination of the spectra from single component particles. Another example for an inorganic mixture of  $\text{NH}_4\text{NO}_3$  and  $\text{K}_2\text{SO}_4$  is provided in Fig. S5Fig. S7. The  $\alpha$ -pinene SOA spectrum is shown in panel (C) of Fig. 4. Ablation of  $\alpha$ -pinene SOA particles forms different types of organic fragments: 1) hydrocarbon and oxygenated organic fragments  $\text{C}_x\text{H}_y\text{O}_z$ , ( $x=1-6$ ,  $y=0-9$ ,  $z=0-3$ , details about the peak assignments can be found in Table S2Table S1), except for  $m/z\ 59^+$ ,  $83^+$ ,  $85^+$ , and  $95^+$ , are comparable to the combination mass spectral patterns for cis-pinonic and pinic acids (refer to Fig. S6Fig. S8) which are oxidation products from  $\alpha$ -pinene ozonolysis (Saathoff et al., 2009; Yu et al., 1999); 2) Carbon clusters  $12\ \text{C}^+$ ,  $24\ \text{C}_2^+$ ,  $36\ \text{C}_3^+$ , and  $60\ \text{C}_5^+$ , with the most prominent peak in  $12\ \text{C}^+$ , assigned to both soot and organic matter fragments in another LAAPTOF study (Ahern et al., 2016); 3) Carboxylic acid groups in the negative spectra, e.g.  $45\ \text{COOH}^-$ ,  $59\ \text{CH}_2\text{COOH}^-$ ,  $73\ \text{C}_2\text{H}_4\text{COOH}^-$ ,  $85\ \text{C}_3\text{H}_4\text{COOH}^-$  and  $99\ \text{C}_4\text{H}_6\text{COOH}^-$ .

Figure 5 (A) shows the spectrum for heterogeneously internally mixed  $\text{K}_2\text{SO}_4$  and PSL particles (PSL core,  $\text{K}_2\text{SO}_4$  shell). All signatures for PSL particles, i.e. hydrocarbon fragments in positive spectra, intensive organic signature  $m/z\ 24^-$ ,  $25^-$ , and  $26^-$ , carbon clusters  $\text{C}_n^{+/-}$ , and  $m/z\ 49^-$  and  $73^-$  fragments arising from unsaturated structures such as aromatic structures are retained in this spectra (grey labels), and the corresponding peak intensities are similar to the pure PSL particles (refer to Fig. S7Fig. S9). However, the intensities of most of the  $\text{K}_2\text{SO}_4$  fragments are weaker compared to pure  $\text{K}_2\text{SO}_4$  particles, likely due to the quite thin or only partial coating layer of  $\text{K}_2\text{SO}_4$  on the PSL core (the nominal geometric size of the PSL particles mixed with the

aqueous solution of  $K_2SO_4$  was 800 nm which is the same size that was selected by the DMA prior to sampling by the mass spectrometer.). The most prominent peak at  $m/z$  39<sup>+</sup> with a normalized intensity of ~0.46, containing both  $K^+$  and  $C_3H_3^+$  fragments, is mainly attributed to  $K^+$  (intensity ~0.73 for pure  $K_2SO_4$ ), since the intensity of  $C_3H_3^+$  (~0.06) for pure PSL is much lower (refer to Fig. S9 Fig. S9). The still intensive signal from 39  $K^+$  despite the weaker sulphate peaks corresponds to the high sensitivity of the instrument for potassium. Fig. 5 (B) shows the average spectrum for poly(allylamine hydrochloride) coated gold particles. Prominent signatures of nitrogen containing compounds (NOCs) ~~is~~ are observed at  $m/z$  58  $C_2H_5-NH-CH_2^+$ , 15  $NH^+$ , 26  $CN^-$ , and 42  $CNO^-$ , as well as the signatures for unsaturated organic compounds at  $m/z$  25<sup>-</sup>, 26<sup>-</sup>, 49<sup>-</sup>, and 73<sup>-</sup>. Strong intensities for  $m/z$  (35<sup>-</sup> plus 36<sup>-</sup>) and 37<sup>-</sup> with ratio a of ~3.1 can be assigned to Cl isotopes derived from the hydrochloride. We also observed small gold peaks at  $m/z$  197<sup>+/-</sup> both in positive and negative spectra.

Mass spectra for other well-defined compounds, i.e. synthetic hematite and pure sea salt particles, are also provided in the supplementary information (Fig. S8 Fig. S10 and S911).

### 3.2.3 Particles consisting of complex mixtures

Figure 6 shows the average spectra for different types of soot particles. All of them show characteristic patterns for elemental carbon (EC)  $C_n^{+/-}$ . For soot1 with high organic carbon (OC) content from propane combustion in the laboratory (panel B), prominent peaks were observed at  $m/z$  28  $CO^+$  and 27  $C_2H_3^+$ , as well as some other organic carbon signatures at  $m/z$  39<sup>+</sup>, 40<sup>+</sup>, 44<sup>+</sup> and 56<sup>+</sup>. All the organic signatures in soot1 with high OC were also observed for soot3, lignocellulosic char from Chestnut wood (panel D), indicating that biomass burning soot contains a significant fraction of OC. It should be noted that biomass burning will also form potassium, thus  $m/z$  39<sup>+</sup> contains both  $K^+$  and  $C_3H_3^+$  fragments.  $M/z$  24<sup>-</sup>, 25<sup>-</sup> and 26<sup>-</sup> can be observed in all the soot types, but with a bit different patterns: 1) soot with high EC content shows very high  $m/z$  24<sup>-</sup> (~2 to 3 times than  $m/z$  25<sup>-</sup>), while 2) soot with high OC shows comparable or even higher  $m/z$  25<sup>-</sup> to than  $m/z$  24<sup>-</sup>. These patterns might provide help to distinguish EC and OC contributions in the spectra from ambient particles.

Figure 7 shows spectra for Arizona test dust (milled desert dust) (~~panel~~ panel A), arable soil SDGe01 sampled from Gottesgabe in Germany (B), and agricultural soil dust collected from harvesting machines after rye and wheat harvest (C). For Arizona test dust, we observed high mineral signatures of aluminium and silicon containing clusters, namely 27  $Al^+$ , 28  $Si^+$ , 44  $SiO^+$ , 43  $AlO^+$ , 59  $AlO_2^+$ , 60  $SiO_2^+$ , 76  $SiO_3^+$ , 119  $AlSiO_4^+$ , 179  $AlSiO_4SiO_2^+$ , 136  $(SiO_2)_2O^+$ . It should be noted that high 16  $O^-$  and 17  $OH^-$  accompany the intensive mineral signatures, attributed to the adsorbed water on the active surface of mineral particles. ~~In addition,~~ In spectra (A), we also observed the following peaks: other mineral related metal clusters, e.g. 7  $Li^+$ , 23  $Na^+$ , 24  $Mg^+$ , 40  $Ca^+$ , 39/41  $K^+$ , 55  $Mn^+$ , 56  $Fe^+$ , 58  $Ni^+$ , 64  $Cu^+$ , metal oxides and hydroxides, e.g. 56  $CaO^+$ , 57  $CaOH^+$ , 96  $Ca_2O^+$ , 112  $(CaO)_2^+$ , and 88  $FeO_2^+$ , as well as weak anion clusters of organic signature ( $m/z$  24  $C_2^-$ , 25  $C_2H^-$ , 26  $C_2H_2^-$ , and 42  $C_2H_2O^-$ ), NOCs ( $m/z$  26  $CN^-$  and 42  $CNO^-$ ), chloride ( $m/z$  35<sup>-</sup> and 37<sup>-</sup>), sulphate ( $m/z$  32<sup>-</sup>, 48<sup>-</sup>, 64<sup>-</sup>, 80<sup>-</sup>, and 97<sup>-</sup>), phosphate (63  $PO_2^-$  and 79  $PO_3^-$ ), diacids (oxalate 89  $(CO)_2OOH^-$  and 117  $(CO)_3OOH^-$ ) and an unknown fragment  $m/z$  148<sup>-</sup> ~~were observed in the spectra (A).~~

$M/z$  26<sup>+</sup> in panels (B) and (C) is much higher than  $m/z$  24<sup>-</sup> and 25<sup>-</sup>, due to the contribution of CN fragments from NOCs. Similar signatures can also be observed in the spectra for Saharan desert dust (Fig. S10 Fig. S12).

~~For soil dust, most~~ Most of their the mineral and organic fragments of soil dust are similar as to those of desert dust, however with different intensities, e.g.  $m/z$  24<sup>-</sup>, 25<sup>-</sup>, 26<sup>-</sup>, and 42<sup>-</sup> (labelled in green) are more intensive than those in desert dust, indicating higher organic compound content. Some peak ratios of fragments are similar across the different dust types, e.g. 40  $Ca^+$  to 56  $CaO^+$  is 2.2, 1.1, and 2 for desert dust, arable soil dust and agricultural soil dust, respectively. Compared with desert dust, there are different fragments from soil dust particles, e.g. EC patterns (labelled in grey), organic acids signatures (blue), ammonium signatures (orange), unsaturated organic fragments ( $m/z$  49<sup>-</sup> and 73<sup>-</sup>) and some other unknown fragments (Weimer et al.). For

Formatiert: Hochgestellt

arable soil dust particles, we also measured samples from Paulinenaue in Germany (SDPA01), Argentina (SDAr08) and Wyoming in USA (SDWY01) (refer to refer to Fig. S11 Fig. S13). Dominant mass spectral peak patterns are similar across all soil dust samples. They are located at around  $m/z$  27<sup>+</sup>, 39<sup>+</sup>, and 56<sup>+</sup> in the positive spectra; and 26<sup>-</sup>, 42<sup>-</sup>, 60<sup>-</sup>, and 76<sup>-</sup> in negative spectra. Less prominent but reproducibly detected are carboxylic acid groups (e.g. COOH<sup>-</sup>) and EC patterns. The German soil dust, however, contains more organic species than soil dust from Argentina and USA, reflected in higher intensities at  $m/z$  24<sup>-</sup>, 25<sup>-</sup>, and 26<sup>-</sup>. Argentinian soil dust contains much less mineral species, expressed in much lower intensities of mineral signatures, e.g.  $m/z$  27<sup>+</sup>, 28<sup>+</sup>, 40<sup>+</sup>, 44<sup>+</sup>, and 56<sup>+</sup>. The German soil dust, however, contains more organic species than the soil dusts from Argentina and the USA, according to since it has reflected in higher the intensities of at  $m/z$  24<sup>-</sup>, 25<sup>-</sup>, and 26<sup>-</sup>, while the Argentinian soil dust contains much less mineral species, due to the expressed in much lower comparing the intensities of mineral signatures, e.g.  $m/z$  27<sup>+</sup>, 28<sup>+</sup>, 40<sup>+</sup>, 44<sup>+</sup>, and 56<sup>+</sup>. The ratios of  $m/z$  39 K<sup>+</sup> and 41 K<sup>+</sup> (3.6, 3.8, 3.5, 5.3 for SDGe01, SDPA01, SDAr08, and SDWY01, respectively) are much lower than the typical peak ratio (~10.6) for potassium (Table 4 Table 2), indicating that they are likely contributed to by both potassium isotopes and hydrocarbon fragments.

For agricultural soil dust particles, obviously ammonium ( $m/z$  18 NH<sub>4</sub><sup>+</sup> and 30 NO<sup>+</sup>), phosphate ( $m/z$  63 PO<sub>2</sub><sup>-</sup>, 79 PO<sub>3</sub><sup>-</sup>, and 95 PO<sub>5</sub><sup>-</sup>) and potassium signatures ( $m/z$  39 K<sup>+</sup> and 41 K<sup>+</sup>) can be found in the spectra, attributed to fertilization. Apart from that, typical biological signatures were observed: 1) the strong  $m/z$  26<sup>-</sup>, 42<sup>-</sup>, and 39<sup>+</sup> pattern is similar to the potassium organo-nitrogen particle type observed by an ATOFMS at an urban site in Barcelona (Dall'Osto et al., 2016), and which were assigned to carbohydrates, arising from biogenic species (Schmidt et al., 2017; Silva et al., 2000). 2) 26<sup>-</sup> and 42<sup>-</sup> could also be contributed by CN<sup>-</sup> and CNO<sup>-</sup> derived from NOCs, i.e. amines, as well as  $m/z$  30 CH<sub>3</sub>NH<sup>+</sup>, 58 C<sub>2</sub>H<sub>5</sub>NHCH<sub>2</sub><sup>+</sup>, and 59 (CH<sub>3</sub>)<sub>3</sub>N<sup>+</sup>. These biological signatures have also been observed by ALABAMA in the field (Schmidt et al., 2017). 3) Some weak but reproducibly detected fragment pattern at around  $m/z$  77 C<sub>6</sub>H<sub>5</sub><sup>+</sup>, 91 C<sub>7</sub>H<sub>7</sub><sup>+</sup>, 103 C<sub>8</sub>H<sub>7</sub><sup>+</sup>, 105 C<sub>8</sub>H<sub>9</sub><sup>+</sup>, and 115 C<sub>9</sub>H<sub>7</sub><sup>+</sup> might be originate from aromatic compounds. Similar patterns can also be found for PSL particles (Fig. S7).

Other examples for complex mixtures, i.e. illite and sea salt particles with biological components are provided in the supplementary information (Fig. S12 Fig. S14 and S9S11).

All the peak assignments and mass spectral patterns like signature peaks as well as some stable peak ratios mentioned above have been summarized in Table S2 Table S1 and Table 4 Table 2, respectively. We consider these laboratory-based reference spectra as useful for the analysis of data obtained also by other LAAPTOF versions and to some extent even for other single particle mass spectrometers. Similar mass spectra are to be expected as long as they use similar ablation & ionization laser pulses (4 mJ, 193 nm), inlet regions for the mass spectrometer, and mass spectrometer types. In the near future, we plan to make these laboratory-based reference spectra publicly available via the EUROCHAMP-2020 data base ([www.eurochamp.org](http://www.eurochamp.org)).

### 3.3 Interpretation of field data

Figure 8 shows an example of bipolar mass spectra for six different particle classes measured in the field campaign at a rural site near Leopoldshafen in southwest Germany. On July 29<sup>th</sup>, 2016 within 24 hours, 7314 particles were detected, successfully ablated and mass spectra generated by LAAPTOF. The 7314 pairs of spectra were then clustered by the Fuzzy c-means algorithm, resulting in six classes. The resulting number of classes with clearly different features depends on the experience of the operating scientist to identify them (please refer to the details of Fuzzy clustering procedure in Procedure 1 in the supplementary information). The Fuzzy results are compared with the laboratory-based reference spectra by calculating their correlation coefficients (cf. Fig. 9). All classes exhibit a sulphate signature with  $m/z$  97 HSO<sub>4</sub><sup>-</sup> and  $m/z$  80 SO<sub>3</sub><sup>-</sup>; a nitrate signature with  $m/z$  46 NO<sub>2</sub><sup>-</sup> and 62 NO<sub>3</sub><sup>-</sup>; an organic compound signature with  $m/z$  24 C<sub>2</sub><sup>-</sup>, 25 C<sub>2</sub>H<sup>-</sup>, and 26 C<sub>2</sub>H<sub>2</sub>/CN<sup>-</sup>; and a NOC signature with  $m/z$  26 CN<sup>-</sup> and 42 CNO<sup>-</sup> in the negative spectra. More characteristic signatures for each particle class can

531 be observed in the positive spectra. All particles measured on this day show a 35% similarity to class 5 with obvious signatures  
532 for potassium (K) and sulphate, with significant correlation with the reference particles containing potassium and sulphate (Fig.  
533 9). Besides, class 5 also has significant correlation with some other cations arising from ammonium, organic compounds, and  
534 dust. The ratio of  $m/z$  ( $39^+ + 40^+$ ) to  $41^+$  is  $\sim 11$ , close to the value for pure  $K_2SO_4$  particles ( $\sim 13.5$ ), thus we assigned them to  $K^+$   
535 rather than organic fragments. Further, there is a 15% similarity to class 4 with prominent ammonium signatures at  $m/z$  18  $NH_4^+$   
536 and 30  $NO^+$ , sulphate signatures, as well as a relatively weaker but reproducible nitrate signature. The corresponding spectrum is  
537 similar as the spectrum for the homogeneous mixtures of  $NH_4NO_3$  and  $(NH_4)_2SO_4$  (panel A in Fig. 4). This class also has strong  
538 correlation with both positive and negative reference spectra for the mixture of ammonium nitrate and ammonium sulphate  
539 particles. Ammonium, nitrate and sulphate are the major secondary inorganic species in atmospheric aerosol particles (Seinfeld  
540 and Pandis, 2006), thus we name this class “secondary inorganic”. It should be noted that this class has significant correlation  
541 with ammonium and cations arising from oxalic acid, however class 4 has weak correlation with the signature cation, i.e.  $m/z$  89  
542  $C_2O_4H^-$  (oxalate), of oxalic acid. Therefore, we can rule out a significant contribution of oxalic acid. There is also a 15%  
543 similarity to class 2 (sodium rich), with a characteristic pattern of a strong signal at  $m/z$  23  $Na^+$  accompanied by two weaker  
544 peaks at  $m/z$  39  $K^+$  (with typical potassium peak ratio of  $\sim 12$ ) and  $63^+$  (might contain both  $Cu^+$  and  $C_5H_3^+$  fragments). Class 2 has  
545 significant correlation with the cations (i.e. Na and K) arising from sea salt, but weak correlation with its anions, such as  $m/z$  35<sup>-</sup>  
546 and 37<sup>-</sup> chloride isotopes. A sea salt contribution can thus be ruled out. Its negative spectrum significantly correlates with nitrate,  
547 sulphate, and dust particles. Besides sodium rich dust aged sea salt may be an appropriate classification. Class 3 is named “aged  
548 soot”, since it has significant correlation with soot particles, especially diesel soot, and a prominent sulphate signal. This class  
549 has an EC pattern with  $m/z$  12n  $C_n^+$ , similar to those in the reference spectra for soot particles (Fig. 6) as well as the reference  
550 spectra for PSL particles (Fig. S9 Fig. S9). The patterns at  $m/z$  27  $C_2H_3^+$  and 28  $CO^+$ ,  $m/z$  36  $C_3^+$  and 39  $C_3H_3^+$  as well as the  $m/z$   
551 24<sup>-</sup>, 25<sup>-</sup> and 26<sup>-</sup> with higher  $m/z$  26<sup>-</sup>, indicate an OC contribution. This is supported by the correlations especially with PSL  
552 particles but also several other organic compounds, suggesting that this class of particles contains organic species. Class 6 is  
553 dominated by calcium (Ca) and sulphate with characteristic calcium signature peaks at  $m/z$  40  $Ca^+$  and 56  $CaO^+$ , also found in the  
554 spectra for dust particles (Fig. 7, Fig. S10 Fig. S12, and S11 S13).  $M/z$  40<sup>+</sup> and 56<sup>+</sup> may also contain 40  $C_2O^+$  and 56  $Fe/C_4H_8^+$   
555 fragments, respectively. Class 1 contains almost all fragments observed in other classes, and is thus named “more aged /mixed  
556 particles”. As shown in Fig. 9, class 6 is consequently correlated with almost all of the reference spectra (both positive and  
557 negative ones).

558 In order to further interpret the field data, we also classified the ambient mass spectra only based on correlation with 17  
559 selected laboratory-based reference spectra (10 positive + 7 negative spectra) listed in Table S3 Table S2. This approach resulted  
560 in 13 particle types, 7 more than were distinguished by Fuzzy clustering. It should be mentioned that at the beginning we were  
561 able to identify all but the Ca rich particle class resulting from Fuzzy clustering, since initially we did not have a reference for  
562 this type. We therefore used class 6 as an additional reference spectrum for this type of particles, which is among one of the 13  
563 types. ~~Initially, using a Pearson’s correlation coefficient  $r$  of  $\geq 0.6$  as threshold for classification resulted in 21 main types of~~  
564 ~~particles (here we use “types” instead of “classes” in order to differentiate these two classification methods), with particle~~  
565 ~~number fractions  $> 1\%$ . The corresponding histogram of these 21 particle types is shown Fig. S13. These 21 types were then~~  
566 ~~manually aggregated after observing their spectra and reduced to 13. Similar as the Fuzzy class number, the resulting number of~~  
567 ~~characteristic types also strongly depends on the expert experience to identify them (please refer to the details of reference~~  
568 ~~spectra oriented grouping procedure in the supplementary information). Their corresponding spectra are shown in Fig. 10. All~~  
569 the types above the dashed line (A to I) exhibit more prominent secondary inorganic signatures ( $m/z$  97  $HSO_4^-$ ) and higher  
570 number fractions than the ones below the dashed line. Although particle types A-I all exhibit a more prominent sulphate pattern

571 with m/z 80 and 97 than nitrate pattern with m/z 46 and 62, they are higher correlated with the mixture of nitrate and sulphate  
572 than either of them. Therefore, we assign the corresponding types to nitrate and sulphate. All the types in the lower panels (J to  
573 M) have significant correlation with arable soil dust in the negative spectra, which have organic signatures, e.g. m/z 24<sup>+</sup>, 25<sup>+</sup>, and  
574 26<sup>+</sup>, as well as some mineral signatures like m/z 119<sup>+</sup>. Compared with the negative spectra, the positive spectra are more  
575 characteristic, which was also observed in the Fuzzy results. Type A, B, C, D, and E are comparable with Fuzzy class 5, 4, 2, 6,  
576 and 3, respectively (the correlation coefficients are 0.89 for type A and class 5, 0.95 for type B and class 4, 0.84 for type C and  
577 class 2, 0.76 for type D and class 6, and 0.81 for type E and class 3). Types F to I are more similar to aged/mixed particles, with  
578 more fragments compared to types A to E. Type H is comparable with Fuzzy class 1. About 10% of the particles cannot be  
579 grouped into any type. This is most likely because of an incorrect mass assignment for the stick spectra, resulting from too large  
580 spectrum-to-spectrum peak shifts for the same ion fragments/clusters which cannot be corrected on a single particle basis with  
581 the existing software (Ramisetty et al., 2017)—10% of the particles cannot be grouped into any type due to spectrum-to-spectrum  
582 peak shifts. As shown in the spectra in both Fig. 9-8 and 10, all organic species were internally mixed with inorganic species.

583 This reference spectra<sub>-</sub>based classification can also be used for identification of particles with low number fractions among  
584 the huge amount of ambient data, and for selection of particles containing particular species e.g. for which the instrument has a  
585 lower sensitivity. This can be achieved by e.g. excluding peaks with high signal such as m/z 39 K/C<sub>3</sub>H<sub>3</sub><sup>+</sup>, or selecting a certain  
586 particle size range, or mass range. As an example, 55 lead containing particles (Pb, with isotopes at m/z 206, 207, and 208)  
587 (details are given in the Procedure 3 in the supplementary information) were identified among the 7314 ambient aerosol particles.  
588 The resulting spectra of particle classes/types in one field study can also be used as reference for other studies. More applications  
589 of these procedures for field data interpretation will be presented in an upcoming paper.

590 In short, Fuzzy and reference spectra<sub>-</sub>based classifications have some comparable results with high correlations (r: 0.76–0.95)  
591 and also have different advantages: Fuzzy classification can identify special ambient particle types without any existing reference  
592 if they have a significant abundance and signal strength, while reference spectra-based methods can identify target particle types  
593 even with little abundance. They are complementary to some extent and thus their combination has the potential to improve  
594 interpretation of field data.

#### 595 4 Conclusions

596 In this study, the overall detection efficiency (ODE) of LAAPTOF was determined to range from  $\sim(0.01 \pm 0.01)\%$  to  $\sim(4.23 \pm$   
597  $2.36)\%$   ~~$\sim(6.57 \pm 2.38)\%$~~  for polystyrene latex (PSL) with the size of 200 to 2000 nm,  $\sim(0.44 \pm 0.19)\%$  to  $\sim(6.57 \pm 2.38)\%$  for  
598 ammonium nitrate (NH<sub>4</sub>NO<sub>3</sub>) and  $\sim(0.14 \pm 0.02)\%$  to  $\sim(1.46 \pm 0.08)\%$  for sodium chloride (NaCl) particles ~~in the size range~~  
599 ~~between 200 and 2000 nm in the size range of 300 to 1000 nm.~~—This is a relative good detection efficiency compared to earlier  
600 versions of the instruments especially when considering the good reproducibility and stability even during field measurements. A  
601 comparison to other single particle mass spectrometers is subject of another study and will be discussed in a separate publication.  
602 ~~In any case in~~Matrix effects from aerosol particles (e.g. size, morphology and optical property) and certain instrument influences  
603 (e.g. aerodynamic lens, detection system) and their interaction must be taken into account to evaluate the LAAPTOF  
604 performance.

605 In order to facilitate the interpretation of single particle mass spectra from field measurements, we have measured various  
606 well defined atmospherically relevant aerosol particles in the laboratory and provide here laboratory-based reference spectra for  
607 aerosol particles of different complexity with comprehensive spectral information about the components (such as organic  
608 compounds, elemental carbon, sulphate, nitrate, ammonium, chloride, mineral compounds, metals, etc. as commonly observed in

609 atmospheric aerosol particles). Our results show that the interpretation of spectra from unknown particle types is significantly  
610 supported by using known mass spectral patterns like signature peaks for ammonium, nitrate, sulphate, and organic compounds  
611 as well as typical peak ratios for e.g. potassium, silicon, and chlorides. Spectra for internally mixed particles may show new  
612 clusters of ions, rather than simply a combination of the ions from single component particles. This may be a complication for  
613 data interpretation which can be overcome if suitable reference spectra for correspondingly mixed particles are available.  
614 Organic compounds generally have some ions in common but exhibit variations depending on the compound. Several peaks can  
615 originate from different fragments; for example, m/z 26<sup>-</sup> and 42<sup>-</sup> could be CN<sup>-</sup> and CNO<sup>-</sup> and/or C<sub>2</sub>H<sub>2</sub><sup>-</sup> and C<sub>2</sub>H<sub>2</sub>O<sup>-</sup>, m/z 39<sup>+</sup> and  
616 41<sup>+</sup> could e.g. originate from K<sup>+</sup> isotopes or organic fragments, and organic matter can also be ionized to form the typical  
617 elemental carbon pattern with C<sub>n</sub><sup>+/-</sup> ions. Hence the interpretation is not always unambiguously possible for such particles but  
618 may require additional information (e.g. size, additional marker peaks, or even higher resolution spectra) or comparison to data  
619 from other instruments like on-line aerosol mass spectrometers (e.g. AMS) or chemical ionization mass spectrometers (e.g.  
620 FIGAERO-CIMS).

621 A set of 7314 mass spectra obtained during one day of field measurements was used for particle type classification by both  
622 Fuzzy clustering and reference spectra. Fuzzy clustering yielded six different classes, which could then be identified with the  
623 help of reference spectra. Classification of the mass spectra based on comparison with 17 reference spectra resulted in 13  
624 different particle types, six of which exhibited high correlation with the Fuzzy clusters (r: 0.76–0.95). Compared with the  
625 reference spectra, we found that each particle class/type has a sulphate signature at m/z 80 SO<sub>3</sub><sup>-</sup> and 97 HSO<sub>4</sub><sup>-</sup>, a nitrate signature  
626 at m/z 46 NO<sub>2</sub><sup>-</sup> and 62 NO<sub>3</sub><sup>-</sup>, an organic compound signature at m/z 24 C<sub>2</sub><sup>-</sup>, 25 C<sub>2</sub>H<sup>-</sup> and 26 C<sub>2</sub>H<sub>2</sub>/CN<sup>-</sup> and a nitrogen-containing  
627 organic signature at m/z 26 CN<sup>-</sup> and 42 CNO<sup>-</sup>. Furthermore, we performed a target-oriented classification by using selected  
628 reference spectra, allowing for the identification of particles with low number fraction in the ambient aerosol, e.g. lead-  
629 containing particles. Based on our results we advise using a combination of both methods for the analysis of SPMS field data.  
630 A set of mass spectra obtained in one day of field measurements was used for particle type classification based on Fuzzy clustering  
631 and on the new reference spectra presented in this work. The corresponding 7314 spectra were clustered by a Fuzzy c-means  
632 algorithm, resulting in six different similarity classes which can be better identified with the help of reference spectra. The  
633 independent classification of the ambient mass spectra based on 17 selected reference spectra resulted in 13 different particle  
634 types, which included including six those classes highly correlated with obtained by Fuzzy clustering results (r: 0.76–0.95).  
635 Compared with the reference spectra, we found that each class has a sulphate signature at m/z 80 SO<sub>3</sub><sup>-</sup> and 97 HSO<sub>4</sub><sup>-</sup>, a nitrate  
636 signature at m/z 46 NO<sub>2</sub><sup>-</sup> and 62 NO<sub>3</sub><sup>-</sup>, an organic compound signature at m/z 24 C<sub>2</sub><sup>-</sup>, 25 C<sub>2</sub>H<sup>-</sup> and 26 C<sub>2</sub>H<sub>2</sub>/CN<sup>-</sup> and a nitrogen-  
637 containing organic signature at m/z 26 CN<sup>-</sup> and 42 CNO<sup>-</sup>. Furthermore, we have performed target-oriented classification by using  
638 a selected reference spectrum, which demonstrates the possibility to identify particles with low number fraction among the huge  
639 amount of ambient data in the ambient aerosol, e.g. lead-containing particles. Taken together, the application of the  
640 mentioned classification methods with complementary features has advanced our understanding of the field measurements.

642 We conclude that the reference spectra presented in this paper are useful for interpretation of field measurements and for  
643 understanding the impact of mixing on typical mass spectral signatures. Furthermore, the reference spectra should be useful for  
644 interpretation of data obtained by other LAAPTOF versions or other single particle mass spectrometers using a similar ionization  
645 method and comparable mass spectrometers. For future experiments using the LAAPTOF, systematic studies on its sensitivity to  
646 different species, distinguishing the organic and inorganic contribution to the same peak in the spectra, and investigating peak  
647 ratios are still required.

Formatiert: Schriftart: Nicht Kursiv, Schriftfarbe: Text 1

Formatiert: Schriftart: Nicht Kursiv, Schriftfarbe: Text 1

Formatiert: Schriftart: Nicht Kursiv, Schriftfarbe: Text 1

Formatiert: Schriftfarbe: Text 1

648 **Data availability**

649 The reference spectra are available upon request from the authors and will be made available in electronic format via the  
650 EUROCHAMP-2020 data base ([www.eurochamp.org](http://www.eurochamp.org)).

651 **Author contributions**

652 X.S. characterised the LAAPTOF, measured all the particles samples, did the data analysis, produced all figures, and wrote the  
653 manuscript. R.R. helped to characterise the LAAPTOF and to measure some of the particle samples. C.M. provided technical and  
654 scientific support for characterising the LAAPTOF as well as data analysis, and for interpretation and discussion of the results.  
655 WH provided scientific support for interpretation and discussion of the results. T.L. gave general advices and comments for this  
656 paper. H.S. provided technical and scientific support for characterising the LAAPTOF, as well as suggestions for the data  
657 analysis, interpretation and discussion. All authors contributed to the final text.

658 **Competing interests**

659 The authors declare that they have no conflicts of interest.

660 **Acknowledgements**

661 The authors gratefully thank the AIDA staff at KIT for helpful discussions and technical support, and the China Scholarship  
662 Council (CSC) for financial support of Xiaoli Shen and Wei Huang. Special thanks go to [Robert Wagner for Mie calculation and](#)  
663 [discussion and comments on the sea salt samples](#), to Thea Schiebel, Kristina Höhler, and Ottmar Möhler for discussions about  
664 the soil dust samples, to Isabelle Steinke for discussions regarding the plant samples, ~~to Robert Wagner for comments on the sea~~  
665 ~~salt samples~~, to Konrad Kandler for providing the Morocco desert dust samples, to Roger Funk and Thomas Hill for providing the  
666 soil dust samples, to Elena Gorokhova and Matt Salter for providing the sea salt with *skeletonema marinoi* culture, and to  
667 Aeromegt GmbH for discussions about the LAAPTOF performance and analysis software.

668 **References**

669 Ackerman, A. A., Adam, J. A., Cairns, B., Cho, H., Gritsevich, M., Jethva, H., Kacenelenbogen, M., Kandler, K., Knobelspiesse,  
670 K., Lanconelli, C., Lupi, A., Mazzola, M., Nousiainen, T., Peltoniemi, J. I., Platnick, S., Puttonen, E., Savenkov, S. N., Segal-  
671 Rosenheimer, M., Sharma, S., Tomasi, C., Torres, O., and Zhang, Z.: Light scattering reviews 9: Light scattering and radiative  
672 transfer, Springer-Praxis, 2015.

673 Ahern, A. T., Subramanian, R., Saliba, G., Lipsky, E. M., Donahue, N. M., and Sullivan, R. C.: Effect of secondary organic  
674 aerosol coating thickness on the real-time detection and characterization of biomass-burning soot by two particle mass  
675 spectrometers, *Atmos Meas Tech*, 9, 6117–6137, 2016.

676 Arndt, J., Sciare, J., Mallet, M., Roberts, G. C., Marchand, N., Sartelet, K., Sellegri, K., Dulac, F., Healy, R. M., and Wenger, J.  
677 C.: Sources and mixing state of summertime background aerosol in the northwestern Mediterranean basin, *Atmos Chem Phys*, 17,  
678 6975–7001, 2016.

679 Bohren, C. F. and Huffman, R. D.: Absorption and scattering of light by small particles, WILEY-VCH Verlag GmbH & Co.  
680 KGaA, 2007.

681 Brands, M., Kamphus, M., Böttger, T., Schneider, J., Drewnick, F., Roth, A., Curtius, J., Voigt, C., Borbon, A., Beekmann, M.,  
682 Bourdon, A., Perrin, T., and Borrmann, S.: Characterization of a newly developed aircraft-based laser ablation aerosol mass  
683 spectrometer (ALABAMA) and first field deployment in urban pollution plumes over Paris during MEGAPOLI 2009, *Aerosol*  
684 *Sci Tech*, 45, 46–64, 2011.

685 Burkholder, J. B., Abbatt, J. P. D., Barnes, I., Roberts, J. M., Melamed, M. L., Ammann, M., Bertram, A. K., Cappa, C. D.,  
686 Carlton, A. G., Carpenter, L. J., Crowley, J. N., Dubowski, Y., George, C., Heard, D. E., Herrmann, H., Keutsch, F. N., Kroll, J.  
687 H., McNeill, V. F., Ng, N. L., Nizkorodov, S. A., Orlando, J. J., Percival, C. J., Picquet-Varrault, B., Rudich, Y., Seakins, P. W.,  
688 Surratt, J. D., Tanimoto, H., Thornton, J. A., Tong, Z., S., T. G., Wahner, A., Weschler, C. J., Wilson, K. R., and Ziemann, P. J.:  
689 The essential role for laboratory studies in atmospheric chemistry, *Environ Sci Technol*, 51, 2519–2528, 2017.

690 Canagaratna, M. R., Jayne, J. T., Jimenez, J. L., Allan, J. D., Alfarra, M. R., Zhang, Q., Onasch, T. B., Drewnick, F., Coe, H.,  
691 Middlebrook, A., Delia, A., Williams, L. R., Trimborn, A. M., Northway, M. J., DeCarlo, P. F., Kolb, C. E., Davidovits, P., and  
692 Worsnop, D. R.: Chemical and microphysical characterization of ambient aerosols with the aerodyne aerosol mass spectrometer,  
693 *Mass Spectrom Rev*, 26, 185–222, 2007.

694 Dall'Osto, M., Beddows, D. C. S., McGillicuddy, E. J., Esser-Gietl, J. K., Harrison, R. M., and Wenger, J. C.: On the  
695 simultaneous deployment of two single-particle mass spectrometers at an urban background and a roadside site during SAPUSS,  
696 *Atmos Chem Phys*, 16, 9693–9710, 2016.

697 Erdmann, N., Dell'Acqua, A., Cavalli, P., Gruning, C., Omenetto, N., Putaud, J. P., Raes, F., and Van Dingenen, R.: Instrument  
698 characterization and first application of the single particle analysis and sizing system (SPASS) for atmospheric aerosols, *Aerosol*  
699 *Sci Tech*, 39, 377–393, 2005.

700 Ervens, B., Feingold, G., Frost, G. J., and Kreidenweis, S. M.: A modeling study of aqueous production of dicarboxylic acids: 1.  
701 Chemical pathways and speciated organic mass production, *J Geophys Res-Atmos*, 109, 2004.

702 Gaie-Levrel, F., Perrier, S., Perraudin, E., Stoll, C., Grand, N., and Schwell, M.: Development and characterization of a single  
703 particle laser ablation mass spectrometer (SPLAM) for organic aerosol studies, *Atmos Meas Tech*, 5, 225–241, 2012.

704 Gard, E., Mayer, J. E., Morrical, B. D., Dienes, T., Fergenson, D. P., and Prather, K. A.: Real-time analysis of individual  
705 atmospheric aerosol particles: Design and performance of a portable ATOFMS, *Anal Chem*, 69, 4083–4091, 1997.

706 Gemayel, R., Hellebust, S., Temime-Roussel, B., Hayeck, N., Van Elteren, J. T., Wortham, H., and Gligorovski, S.: The  
707 performance and the characterization of laser ablation aerosol particle time-of-flight mass spectrometry (LAAP-ToF-MS), *Atmos*  
708 *Meas Tech*, 9, 1947–1959, 2016.

709 Gross, D. S., Gälli, M. E., Silva, P. J., and Prather, K. A.: Relative sensitivity factors for alkali metal and ammonium cations in  
710 single particle aerosol time-of-flight mass spectra, *Anal Chem*, 72, 416–422, 2000.

711 Hagemann, R., Corsmeier, U., Kottmeier, C., Rinke, R., Wieser, A., and Vogel, B.: Spatial variability of particle number  
712 concentrations and NO<sub>x</sub> in the Karlsruhe (Germany) area obtained with the mobile laboratory 'AERO-TRAM', *Atmos Environ*,  
713 94, 341–352, 2014.

714 Hinz, K. P., Greweling, M., Drews, F., and Spengler, B.: Data processing in on-line laser mass spectrometry of inorganic,  
715 organic, or biological airborne particles, *J Am Soc Mass Spectr*, 10, 648–660, 1999.

716 Jimenez, J. L., Canagaratna, M. R., Donahue, N. M., Prevot, A. S. H., Zhang, Q., Kroll, J. H., DeCarlo, P. F., Allan, J. D., Coe,  
717 H., Ng, N. L., Aiken, A. C., Docherty, K. S., Ulbrich, I. M., Grieshop, A. P., Robinson, A. L., Duplissy, J., Smith, J. D., Wilson,  
718 K. R., Lanz, V. A., Hueglin, C., Sun, Y. L., Tian, J., Laaksonen, A., Raatikainen, T., Rautiainen, J., Vaattovaara, P., Ehn, M.,  
719 Kulmala, M., Tomlinson, J. M., Collins, D. R., Cubison, M. J., Dunlea, E. J., Huffman, J. A., Onasch, T. B., Alfarra, M. R.,  
720 Williams, P. I., Bower, K., Kondo, Y., Schneider, J., Drewnick, F., Borrmann, S., Weimer, S., Demerjian, K., Salcedo, D.,  
721 Cottrell, L., Griffin, R., Takami, A., Miyoshi, T., Hatakeyama, S., Shimono, A., Sun, J. Y., Zhang, Y. M., Dzepina, K., Kimmel,  
722 J. R., Sueper, D., Jayne, J. T., Herndon, S. C., Trimborn, A. M., Williams, L. R., Wood, E. C., Middlebrook, A. M., Kolb, C. E.,  
723 Baltensperger, U., and Worsnop, D. R.: Evolution of organic aerosols in the atmosphere, *Science*, 326, 1525–1529, 2009.

724 Johnston, M. V.: Sampling and analysis of individual particles by aerosol mass spectrometry, *J Mass Spectrom*, 35, 585–595,  
725 2000.

726 Kamphus, M., Ettner-Mahl, M., Brands, M., Curtius, J., Drewnick, F., and Borrmann, S.: Comparison of two aerodynamic lenses  
727 as an inlet for a single particle laser ablation mass spectrometer, *Aerosol Sci Tech*, 42, 970–980, 2008.

728 Kulkarni, P., Baron, P. A., and Willeke, K.: *Aerosol measurement: Principles, techniques, and applications*, John Wiley & Sons,  
729 Inc., 2011.

730 Li, L., Huang, Z. X., Dong, J. G., Li, M., Gao, W., Nian, H. Q., Fu, Z., Zhang, G. H., Bi, X. H., Cheng, P., and Zhou, Z.: Real  
731 time bipolar time-of-flight mass spectrometer for analyzing single aerosol particles, *Int J Mass Spectrom*, 303, 118–124, 2011.

732 Li, W., Sun, J., Xu, I., Shi, Z., Riemer, N., Sun, Y., Fu, P., Zhang, J., Lin, Y., Wang, X., Shao, L., Chen, J., Zhang, X., Wang, Z.,  
733 and Wang, W.: A conceptual framework for mixing structures in individual aerosol particles, *J Geophys Res-Atmos*, 121,  
734 13784–13798, 2016.

735 Lin, Q. H., Zhang, G. H., Peng, L., Bi, X. H., Wang, X. M., Brechtel, F. J., Li, M., Chen, D. H., Peng, P. A., Sheng, G. Y., and  
736 Zhou, Z.: In situ chemical composition measurement of individual cloud residue particles at a mountain site, southern China,  
737 *Atmos Chem Phys*, 17, 2017.

738 Liu, P., Ziemann, P. J., Kittelson, D. B., and McMurry, P. H.: Generating Particle Beams of Controlled Dimensions and  
739 Divergence .2. Experimental Evaluation of Particle Motion in Aerodynamic Lenses and Nozzle Expansions, *Aerosol Sci Tech*,  
740 22, 314–324, 1995.

741 Marsden, N., Flynn, M. J., Allan, J. D., and Coe, H.: On-line differentiation of mineral phase in aerosol particles by ion formation  
742 mechanism using a LAAP-TOF single particle mass spectrometer, *Atmos Meas Tech Discuss*, doi: 10.5194/amt-2017-85, 2017.

743 Marsden, N., Flynn, M. J., Taylor, J. W., Allan, J. D., and Coe, H.: Evaluating the influence of laser wavelength and detection  
744 stage geometry on optical detection efficiency in a single-particle mass spectrometer, *Atmos Meas Tech*, 9, 6051–6068, 2016.

745 Moffet, R. C., de Foy, B., Molina, L. T., Molina, M. J., and Prather, K. A.: Measurement of ambient aerosols in northern Mexico  
746 City by single particle mass spectrometry, *Atmos Chem Phys*, 8, 4499–4516, 2008.

747 Murphy, D. M.: The design of single particle laser mass spectrometers, *Mass Spectrom Rev*, 26, 150–165, 2007.

748 Murphy, D. M., Cziczko, D. J., Froyd, K. D., Hudson, P. K., Matthew, B. M., Middlebrook, A. M., Peltier, R. E., Sullivan, A.,  
749 Thomson, D. S., and Weber, R. J.: Single-particle mass spectrometry of tropospheric aerosol particles, *J Geophys Res-Atmos*,  
750 111, 2006.

751 Murphy, D. M., Middlebrook, A. M., and Warshawsky, M.: Cluster analysis of data from the Particle Analysis by Laser Mass  
752 Spectrometry (PALMS) instrument, *Aerosol Sci Tech*, 37, 382–391, 2003.

753 Murphy, D. M. and Thomson, D. S.: Laser ionization mass-spectroscopy of single aerosol-particles, *Aerosol Sci Tech*, 22, 237–  
754 249, 1995.

755 Noble, C. A. and Prather, K. A.: Real-time single particle mass spectrometry: a historical review of a quarter century of the  
756 chemical analysis of aerosols, *Mass Spectrom Rev*, 19, 248–274, 2000.

757 Pöschl, U.: Atmospheric aerosols: Composition, transformation, climate and health effects, *Angew Chem Int Edit*, 44, 7520–  
758 7540, 2005.

759 Pratt, K. A. and Prather, K. A.: Mass spectrometry of atmospheric aerosols-Recent developments and applications. Part II: On-  
760 line mass spectrometry techniques, *Mass Spectrom Rev*, 31, 17–48, 2012.

761 Ramisetty, R., Abdelmonem, A., Shen, X., Saathoff, H., Mohr, C., and Leisner, T.: Comparison of nanosecond and femtosecond  
762 laser ablation in single particle mass spectrometer for atmospheric applications, *Atmos Meas Tech Discuss*, doi.org/10.5194/amt-  
763 2017-357, 2017.

764 Reitz, P., Zorn, S. R., Trimborn, S. H., and Trimborn, A. M.: A new, powerful technique to analyze single particle aerosol mass  
765 spectra using a combination of OPTICS and the fuzzy c-means algorithm, *J Aerosol Sci*, 98, 1–14, 2016.

766 Roth, A., Schneider, J., Klimach, T., Mertes, S., van Pinxteren, D., Herrmann, H., and Borrmann, S.: Aerosol properties, source  
767 identification, and cloud processing in orographic clouds measured by single particle mass spectrometry on a central European  
768 mountain site during HCCT-2010, *Atmos Chem Phys*, 16, 505–524, 2016.

769 Saathoff, H., Möhler, O., Schurath, U., Kamm, S., Dippel, B., and Mihelcic, D.: The AIDA soot aerosol characterisation  
770 campaign 1999, *J Aerosol Sci*, 34, 1277–1296, 2003.

771 Saathoff, H., Naumann, K. H., Möhler, O., Jonsson, A. M., Hallquist, M., Kiendler-Scharr, A., Mentel, T. F., Tillmann, R., and  
772 Schurath, U.: Temperature dependence of yields of secondary organic aerosols from the ozonolysis of  $\alpha$ -pinene and limonene,  
773 *Atmos Chem Phys*, 9, 1551–1577, 2009.

774 Schill, G. P. and Tolbert, M. A.: Heterogeneous ice nucleation on phase-separated organic-sulfate particles: effect of liquid vs.  
775 glassy coatings, *Atmos Chem Phys*, 13, 4681–4695, 2013.

776 Schmidt, S., Schneider, J., Klimach, T., Mertes, S., Schenk, L. P., Curtius, J., and Borrmann, S.: Online single particle analysis  
777 of ice particle residuals from mountain-top mixed-phase clouds using laboratory derived particle type assignment, *Atmos Chem*  
778 *Phys*, 17, 575–594, 2017.

779 Schreiner, J., Schild, U., Voigt, C., and Mauersberger, K.: Focusing of aerosols into a particle beam at pressures from 10 to 150  
780 Torr, *Aerosol Sci Tech*, 31, 373–382, 1999.

781 Seinfeld, J. H. and Pandis, S. N.: *Atmospheric chemistry and physics: From air pollution to climate change*, Wiley, J & Sons,  
782 Inc., Hoboken, New Jersey, 2006.

783 Silva, P. J., Carlin, R. A., and Prather, K. A.: Single particle analysis of suspended soil dust from Southern California, *Atmos*  
784 *Environ*, 34, 1811–1820, 2000.

785 Su, Y. X., Sipin, M. F., Furutani, H., and Prather, K. A.: Development and characterization of an aerosol time-of-flight mass  
786 spectrometer with increased detection efficiency, *Anal Chem*, 76, 712–719, 2004.

787 Trimborn, A., Hinz, K.-P., and Spengler, B.: Online analysis of atmospheric particles with a transportable laser mass  
788 spectrometer, *Aerosol Sci Tech*, 33, 191–201, 2000.

789 Tsigaridis, K., Krol, M., Dentener, F. J., Balkanski, Y., Lathièrè, J., Metzger, S., Hauglustaine, D. A., and Kanakidou, M.:  
790 Change in global aerosol composition since preindustrial times, *Atmos Chem Phys*, 6, 5143–5162, 2006.

791 Usher, C. R., Michel, A. E., and Grassian, V. H.: Reactions on mineral dust, *Chem Rev*, 103, 4883–4939, 2003.

792 Wagner, R., Kaufmann, J., Möhler, O., Saathoff, H., Schnaiter, M., Ullrich, R., and Leisner, T.: Heterogeneous ice nucleation  
793 ability of NaCl and sea salt aerosol particles at cirrus temperatures, *J. Geophys. Res. (Atmos.)* (in preparation), 2017.

794 Weimer, M., Schröter, J., Eckstein, J., Deetz, K., Neumaier, M., Fischbeck, G., Hu, L., Millet, D. B., Rieger, D., Vogel, H.,  
795 Vogel, B., Reddmann, T., Kirner, O., Ruhnke, R., and Braesicke, P.: An emission module for ICON-ART 2.0: implementation  
796 and simulations of acetone, *Geosci Model Dev*, 10, 2471–2494, 2017.

797 Williams, L. R., Gonzalez, L. A., Peck, J., Trimborn, D., McInnis, J., Farrar, M. R., Moore, K. D., Jayne, J. T., Robinson, W. A.,  
798 Lewis, D. K., Onasch, T. B., Canagaratna, M. R., Trimborn, A., Timko, M. T., Magoon, G., Deng, R., Tang, D., Blanco, E. D. L.  
799 R., Prévôt, A. S. H., Smith, K. A., and Worsnop, D. R.: Characterization of an aerodynamic lens for transmitting particles greater  
800 than 1 micrometer in diameter into the Aerodyne aerosol mass spectrometer, *Atmos Meas Tech*, 6, 3271–3280, 2013.

801 Wonaschuetz, A., Kallinger, P., Szymanski, W., and Hitzenberger, R.: Chemical composition of radiolytically formed particles  
802 using single-particle mass spectrometry, *J Aerosol Sci*, 113, 242–249, 2017.

803 Yu, J. Z., Cocker, D. R., Griffin, R. J., Flagan, R. C., and Seinfeld, J. H.: Gas-phase ozone oxidation of monoterpenes: Gaseous  
804 and particulate products, *J. Atmos. Chem.*, 34, 207–258, 1999.

805 Zawadowicz, M. A., Abdelmonem, A., Mohr, C., Saathoff, H., Froyd, K. D., Murphy, D. M., Leisner, T., and Cziczo, D. J.:  
806 Single-particle time-of-flight mass spectrometry utilizing a femtosecond desorption and ionization laser, *Anal Chem*, 87, 12221–  
807 12229, 2015.

808 Zawadowicz, M. A., Lance, S., Jayne, J. T., Croteau, P., Worsnop, D. R., Mahrt, F., Leisner, T., and Cziczo, D. J.: Quantifying  
809 and improving the performance of the Laser Ablation Aerosol Particle Time of Flight Mass Spectrometer (LAAPTof)  
810 instrument, *Atmos Meas Tech Discuss*, doi: 10.5194/amt-2017-1, 2017.

811 Zelenyuk, A., Cai, Y., and Imre, D.: From agglomerates of spheres to irregularly shaped particles: Determination of dynamic  
812 shape factors from measurements of mobility and vacuum aerodynamic diameters, *Aerosol Sci Tech*, 40, 197–217, 2006a.

813 Zelenyuk, A. and Imre, D.: Single particle laser ablation time-of-flight mass spectrometer: An introduction to SPLAT, *Aerosol  
814 Sci Tech*, 39, 554–568, 2005.

815 Zelenyuk, A., Imre, D., Cai, Y., Mueller, K., Han, Y. P., and Imrich, P.: SpectraMiner, an interactive data mining and  
816 visualization software for single particle mass spectroscopy: A laboratory test case, *Int J Mass Spectrom*, 258, 58–73, 2006b.

817 Zelenyuk, A., Yang, J., Choi, E., and Imre, D.: SPLAT II: An aircraft compatible, ultra-sensitive, high precision instrument for  
818 in-situ characterization of the size and composition of fine and ultrafine particles, *Aerosol Sci Tech*, 43, 411–424, 2009.

819 Zhang, Q., Jimenez, J. L., Canagaratna, M. R., Allan, J. D., Coe, H., Ulbrich, I., Alfarra, M. R., Takami, A., Middlebrook, A. M.,  
820 Sun, Y. L., Dzepina, K., Dunlea, E., Docherty, K., DeCarlo, P. F., Salcedo, D., Onasch, T., Jayne, J. T., Miyoshi, T., Shimo  
821 o, A., Hatakeyama, S., Takegawa, N., Kondo, Y., Schneider, J., Drewnick, F., Borrmann, S., Weimer, S., Demerjian, K., Williams,  
822 P., Bower, K., Bahreini, R., Cottrell, L., Griffin, R. J., Rautiainen, J., Sun, J. Y., Zhang, Y. M., and Worsnop, D. R.: Ubiquity  
823 and dominance of oxygenated species in organic aerosols in anthropogenically-influenced Northern Hemisphere midlatitudes,  
824 *Geophys Res Lett*, 34, 2007.

825 Zhao, W. X., Hopke, P. K., and Prather, K. A.: Comparison of two cluster analysis methods using single particle mass spectra,  
826 *Atmos Environ*, 42, 881–892, 2008.

827

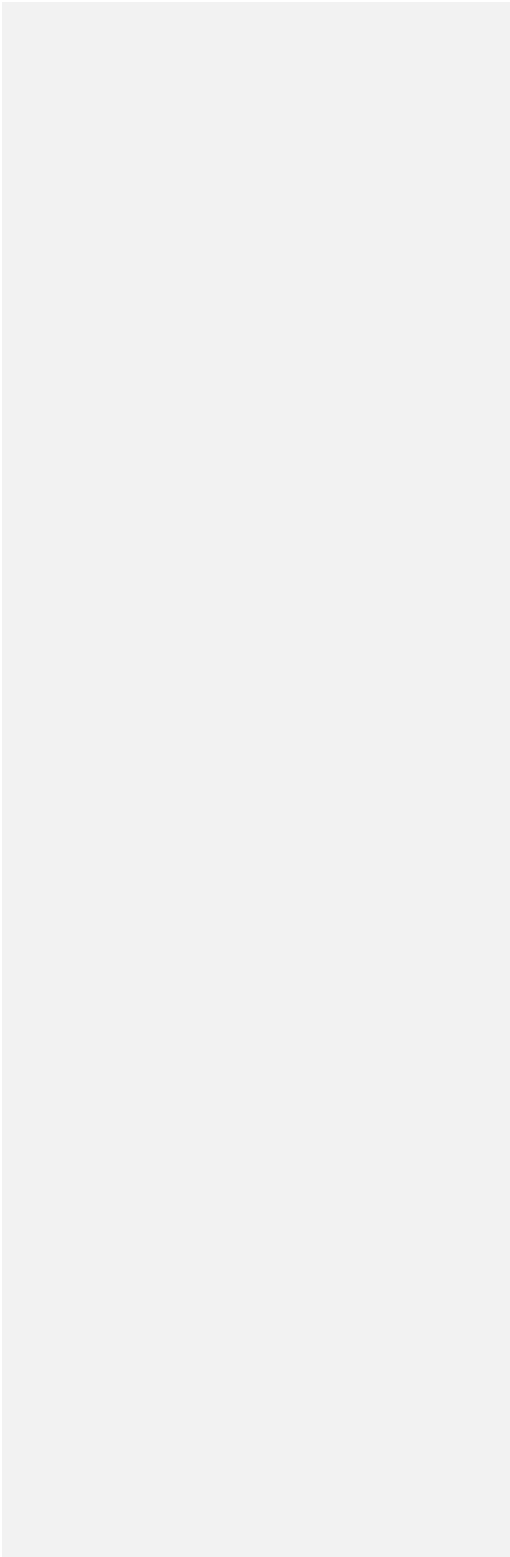
Formatiert: Ebene 4

Table 1: Overview of laboratory generated aerosol particles for reference mass spectra

Aerosol particle types	Size/nm		Morphology	Source	Generation method	No. of spectra
	$d_{va}$	width <sup>a</sup>				
<b>1. Particles consisting of pure compounds</b>						
- Ammonium nitrate, NH <sub>4</sub> NO <sub>3</sub>	1160	101	aspherical	≥ 99.5%, Fluka	A	497
- Ammonium sulphate <sup>b</sup> , (NH <sub>4</sub> ) <sub>2</sub> SO <sub>4</sub>	611	79	aspherical	≥ 99.5%, Merck	A	537
- Potassium sulphate, K <sub>2</sub> SO <sub>4</sub>	1465	232	aspherical	≥ 99%, Merck	A	300
- Sodium chloride, NaCl	1202	133	cubic	≥ 99.5%, Merck	A	250
- Silica, SiO <sub>2</sub> (Glass beads)	2097	44	spherical	Palas GmbH	S	347
- Oxalic acid, C <sub>2</sub> H <sub>2</sub> O <sub>4</sub>	1081	322	spherical	Merck	A	773
- Pinic acid, C <sub>9</sub> H <sub>14</sub> O <sub>4</sub>	902	94	spherical	University of Mainz	A	683
- Cis-pinonic acid, C <sub>10</sub> H <sub>16</sub> O <sub>3</sub>	702	88	spherical	98%, ACROS ORGANICS	A	600
- Humic acid	1221	126	spherical	100%, Alfa Aesar	A	773
- Polystyrene latex (PSL)	818	3	spherical	Thermo scientific	A	235
<b>2. Particles consisting of well-defined mixtures</b>						
- Ammonium nitrate & ammonium sulfate (mass ratio = 1:1)	1102	165	aspherical	single component samples are from the same source	A	454
- Potassium sulfate & sodium chloride (mass ratio = 1:1)	1375	197	aspherical	as the corresponding pure compounds		259
- Ammonium nitrate & potassium sulfate (mass ratio = 2:1)	854	112	aspherical			576
- Hematite	1091	817	spherical	Karlsruhe Institute of Technology (KIT)	S	320
- Pure sea salt	1205	218	cubic	Sigma Aldrich	B1	422
- $\alpha$ -Pinene secondary organic aerosols (SOA)	505	84	spherical	(1S)-(-)- $\alpha$ -pinene (99%) from Aldrich	B1 <sup>c</sup>	1938
- Potassium sulfate coated PSL	805	58	partially coated	Merck & Thermo scientific	A	609
- Poly(allylamine hydrochloride) coated gold	400 <sup>d</sup>		300 nm core-50 nm shell	Nanopartz Inc.	Nebulized without sizing	417
<b>3. Particles consisting of complex mixtures</b>						
- Soot1 with low organic carbon	386 <sup>e</sup>	275	agglomerates	incomplete combustion of propane, C/O=0.29	B2	617
- Soot1 with high organic carbon	120 <sup>e</sup>	58	agglomerates	incomplete combustion of propane, C/O=0.54	B2	347
- Soot2 Lignocellulosic char	828	766	agglomerates	Lignocellulosic char from Chestnut wood; University of Zürich, Switzerland	S	390
- Soot3 Diesel particles	624+980 <sup>f</sup>		agglomerates	NIST (2975)	S	533
- Arizona test dust	1169	874	aspherical	Powder Technology Inc.	S	261
- Saharan desert dust 1 (Morocco)	890	1230	aspherical	Konrad Kandler, TU Darmstadt	S	338
- Saharan desert dust 2 (Cairo)	1334±1454 <sup>f</sup>		aspherical	Khaled Megahed, KIT	S	396
- Arable soil dust SDGe01 (Gottesgabe, Germany)	912	392	aspherical	Roger Funk <sup>g</sup>	B1 <sup>h</sup>	583
- Arable soil dust SDPA01 (Paulinenaue, Germany)	787	334	aspherical	Roger Funk <sup>g</sup>	B1 <sup>h</sup>	385
- Arable soil dust SDAr08 (Argentina)	910	407	aspherical	Roger Funk <sup>g</sup>	B1 <sup>h</sup>	592
- Arable soil dust SDWY01 (Wyoming, USA)	864	430	aspherical	Tom Hill <sup>i</sup>	B1 <sup>h</sup>	623
- Agricultural soil dust (Northern Germany)	561	249	aspherical	Roger Funk <sup>g</sup>	B1 <sup>h</sup>	583
- Urban dust	1329	1266	aspherical	NIST(1649a)	S	375
- Illite NX	825	260	sheet	Arginotec	S	807
- Sea salt with skeletonema marinoi <sup>j</sup>	1212	338	cubic	Matt Salter <sup>j</sup>	B1	526

Formatierte Tabelle

829 Note: For aerosol generation methods:  
830 “A” represents for the method by using a nebulizer and a DMA (refer to the setup in Fig. 1) for sizing  $d_m=800$  nm;  
831 “B1” and “B2” represent the methods in which particles were sampled from AIDA and a stainless steel cylinder, respectively;  
832 “S” corresponds to particles mobilized by shaking in a reservoir.  
833 For particles size information,  $d_{va}$  values represent the expected values from Gaussian fitting to the particle sizes measured by LAAPTOF.  
834 Spectra number is the number of averaged spectra.  
835 <sup>a</sup>: These values represent the standard deviation from Gaussian fitting to the measured particle sizes ( $d_{va}$ ).  
836 <sup>b</sup>: There is only one weak but reproducible peak m/z 30 NO<sup>+</sup> in the positive spectra. Therefore we don't give the reference spectra in this paper.  
837 <sup>c</sup>: SOA particles were formed in the Aerosol Preparation and Characterization (APC) chamber and then transferred into the AIDA chamber.  
838 <sup>d</sup>: The nominal geometric size given by the manufacture Nanopartz Inc.  
839 <sup>e</sup>: Electrical mobility equivalent diameter,  $d_m$ , measured by a scanning mobility particle sizer (SMPS).  
840 <sup>f</sup>: The sizes ( $d_{va}$ ) of Diesel particles and Saharan desert dust 2 are average values with their standard deviation.  
841 <sup>g</sup>: Institute of Soil Landscape Research, Leibniz Centre for Agricultural Landscape Research, Germany.  
842 <sup>h</sup>: Soil dust samples were dispersed by a rotating brush generator and injected via cyclones into the AIDA chamber.  
843 <sup>i</sup>: Department of Atmospheric Science, Colorado State University, Fort Collins, Colorado, USA.  
844 <sup>j</sup>: Samples, provided by Elena Gorokhova and Matt Salter at Stockholm University, they were prepared by diluting a pure *skeletonema marinoi*  
845 culture with artificial seawater (sigma sea salt) to conditions representative of a bloom in the ocean.  
846



848

Formatiert: Standard

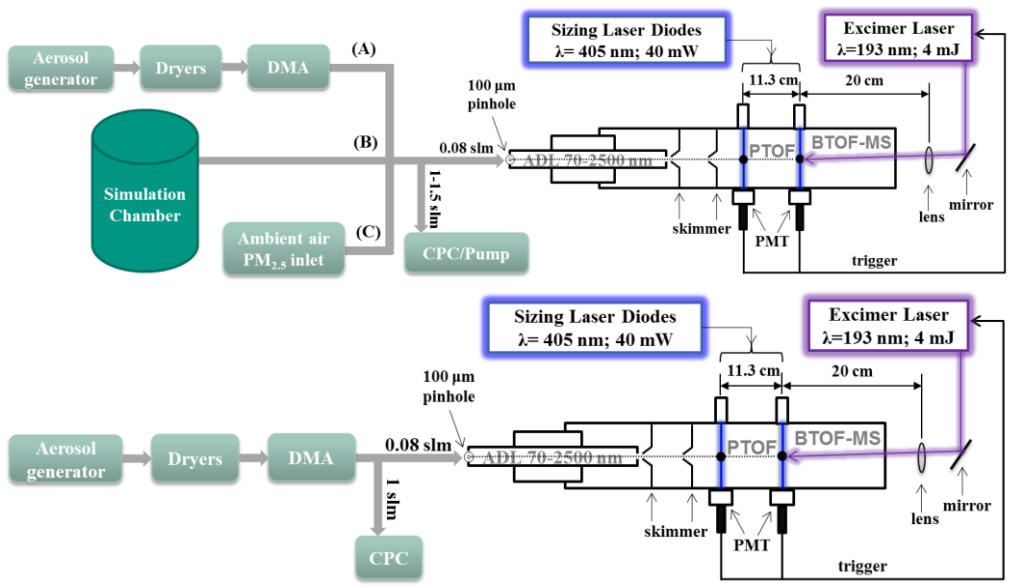
849 **Table 1/ Table 2: Summary of mass spectral patterns**

Species	Signature peaks in positive spectra	Signature peaks in negative spectra	Typical Peak Ratios histogram $x_0$ (width)*
potassium	39 K <sup>+</sup> , 41 K <sup>+</sup>		(I39+I40):I41= <b>~13.5</b> (0.9)
calcium	40 Ca <sup>+</sup> , 56 CaO <sup>+</sup>		
aluminium	27 Al <sup>+</sup>	43 AlO <sup>-</sup> , 59 AlO <sub>2</sub> <sup>-</sup>	
silicon	28 Si <sup>+</sup> , 44 SiO <sup>+</sup>	60 SiO <sub>2</sub> <sup>-</sup> , 76 SiO <sub>3</sub> <sup>-</sup> , 77 HSiO <sub>3</sub> <sup>-</sup>	(I76+I77):I60= <b>~1.0</b> (0.33)
silicon & aluminium	27 Al <sup>+</sup> , 28 Si <sup>+</sup> , 44 SiO <sup>+</sup>	43 AlO <sup>-</sup> , 59 AlO <sub>2</sub> <sup>-</sup> , 60 SiO <sub>2</sub> <sup>-</sup> , 76 SiO <sub>3</sub> <sup>-</sup> , 77 HSiO <sub>3</sub> <sup>-</sup> , 119 AlSiO <sub>4</sub> <sup>-</sup> , 179 AlSiO <sub>4</sub> .SiO <sub>2</sub> <sup>-</sup>	
ammonium	18 NH <sub>4</sub> /H <sub>2</sub> O <sup>+</sup> , 30 NO <sup>+</sup>		
nitrate	30 NO <sup>+</sup>	46 NO <sub>2</sub> <sup>-</sup> , 62 NO <sub>3</sub> <sup>-</sup>	
sulphate		32 S <sup>-</sup> , 48 SO <sup>-</sup> , 64 SO <sub>2</sub> <sup>-</sup> , 80 SO <sub>3</sub> <sup>-</sup> , 81HSO <sub>3</sub> <sup>-</sup> , 96 SO <sub>4</sub> <sup>-</sup> , 97 HSO <sub>4</sub> <sup>-</sup> ,	
chloride		35 Cl <sup>-</sup> , 37 Cl <sup>-</sup>	(I35+I36):I37= <b>~3.21</b> (0.95)
elemental carbon	12 <sub>n</sub> C <sub>n</sub> <sup>+</sup>	12 <sub>n</sub> C <sub>n</sub> <sup>-</sup>	
organics		24 C <sub>2</sub> <sup>-</sup> , 25 C <sub>2</sub> H <sup>-</sup> , 26 C <sub>2</sub> H <sub>2</sub> CN <sup>-</sup>	
organic acids		45 COOH <sup>-</sup> , 59 CH <sub>2</sub> COOH <sup>-</sup> , 71 CCH <sub>2</sub> COOH <sup>-</sup> , 73 C <sub>2</sub> H <sub>4</sub> COOH <sup>-</sup> , 85 C <sub>3</sub> H <sub>4</sub> COOH <sup>-</sup> , 99 C <sub>4</sub> H <sub>6</sub> COOH <sup>-</sup> , 117 (CO) <sub>3</sub> OOH <sup>-</sup>	
nitrogen-containing organics		26 CN <sup>-</sup> , 42 CNO <sup>-</sup>	
unsaturated organics		25 C <sub>2</sub> H <sup>-</sup> , 26 C <sub>2</sub> H <sub>2</sub> <sup>-</sup> unknown fragments 49- and 73-	
aromatic compounds	77 C <sub>6</sub> H <sub>5</sub> <sup>+</sup> , 91C <sub>7</sub> H <sub>7</sub> <sup>+</sup> , 103 C <sub>8</sub> H <sub>7</sub> <sup>+</sup> /105 C <sub>8</sub> H <sub>9</sub> <sup>+</sup> , 115 C <sub>9</sub> H <sub>7</sub> <sup>+</sup>	25 C <sub>2</sub> H <sup>-</sup> , 26 C <sub>2</sub> H <sub>2</sub> <sup>-</sup> unknown fragments 49- and 73-	

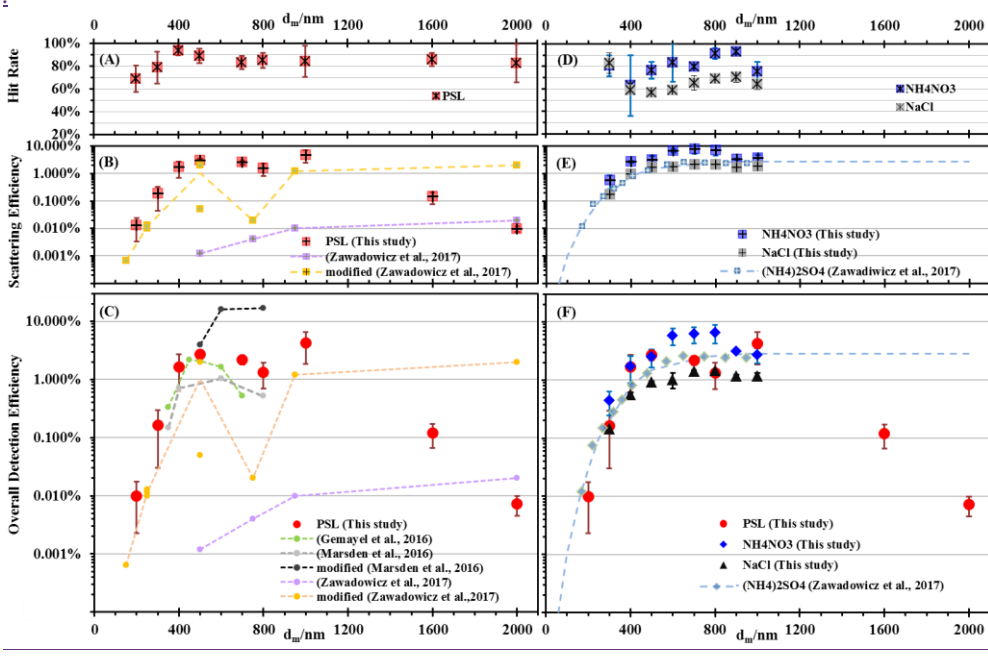
850

851 Note:

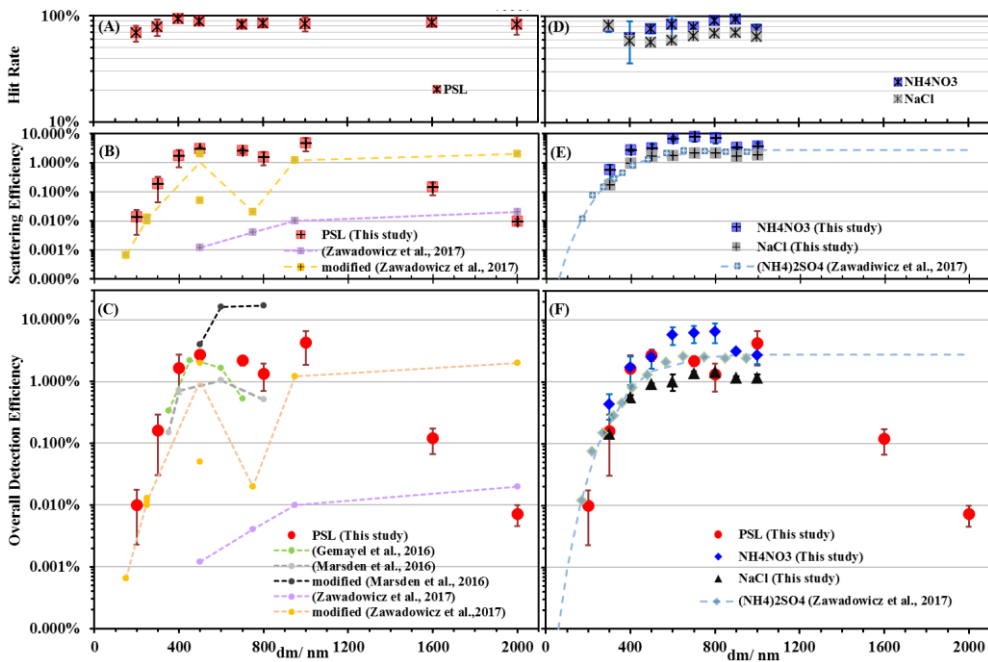
852 \*We have made histograms for the three typical peak ratios, respectively (ref. Fig-S3Fig. S5). Histogram  $x_0$  is the expected value that indicates  
853 the position of the peak resulting from Gaussian fit, and the width is the corresponding standard deviation. I is short for the intensity of the  
854 corresponding peak in LAAPTOF spectra; typical peak ratios for potassium and chloride are based on pure and mixed salt that containing K  
855 and Cl; typical peak ratios for silicon are based on pure SiO<sub>2</sub>.



858  
859  
860  
861  
862  
863  
864  
Figure 1: Schematic of the LAAPTOF instrument and three different experimental setups for measuring standard samples (method A); setup (A) e.g. PSL, NH<sub>4</sub>NO<sub>3</sub> and K<sub>2</sub>SO<sub>4</sub> particles, which were generated from a nebulizer, passed through two dryers, were size-selected by a differential mobility analyzer (DMA), and then measured by LAAPTOF; setup (B) was used for samples generated in or dispersed into the AIDA chamber (~84.5 m<sup>3</sup>) or samples dispersed into a stainless steel cylinder (~0.18 m<sup>3</sup>); setup (C) was used for measuring ambient aerosols in field campaigns. In addition, some particles, e.g. mineral dust, were sampled directly from the headspace of their reservoirs.



Formatiert: Keine



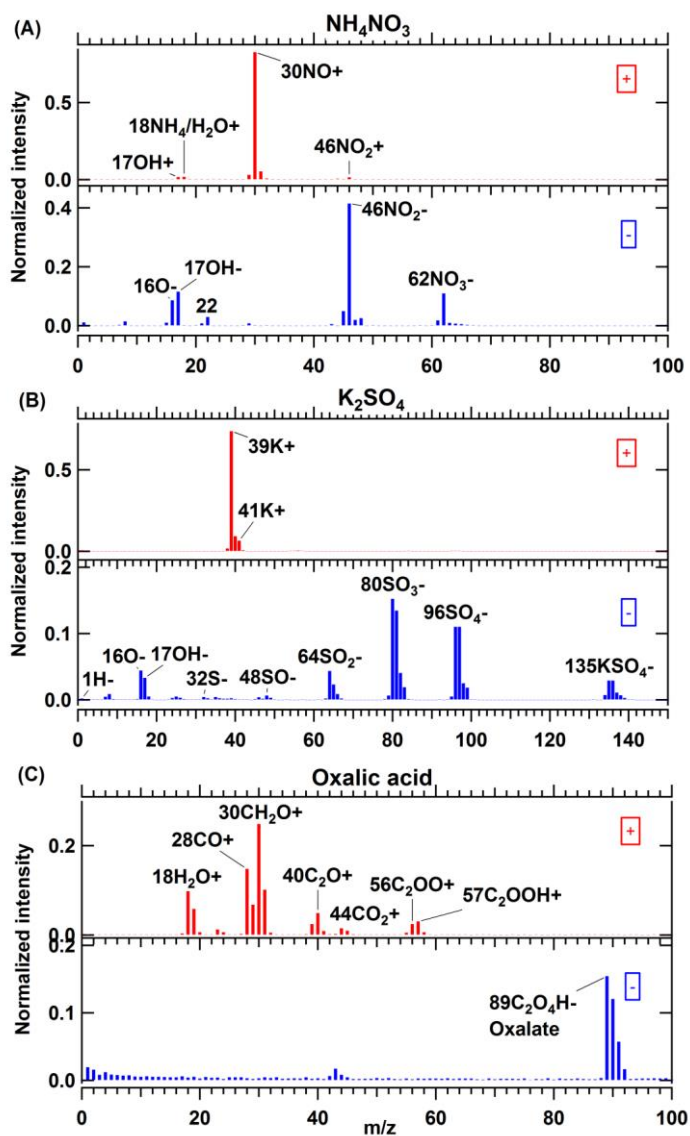
Formatiert: Beschriftung, Links, Zeilenabstand: einfach

867

868  
869  
870  
871  
872  
873  
874

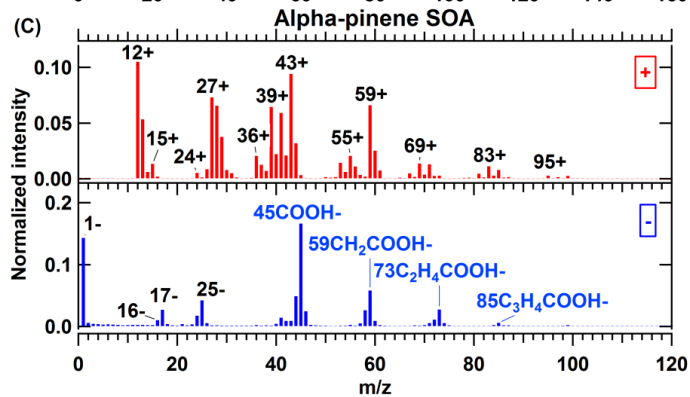
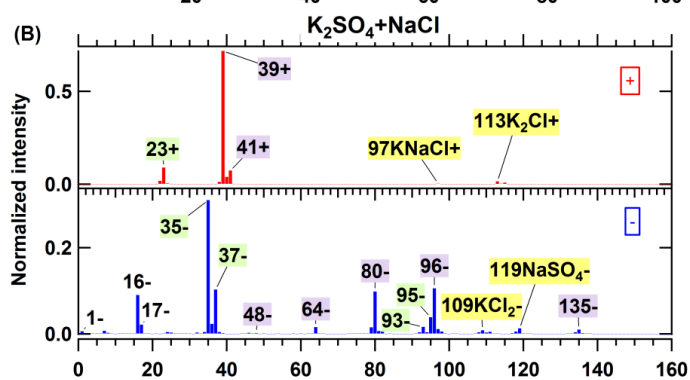
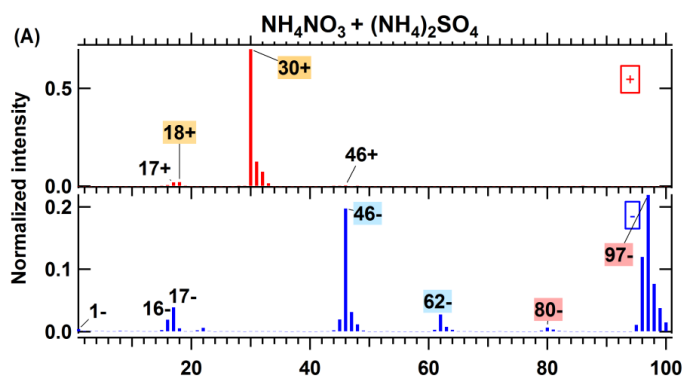
Figure 2: Hit rate (HR, panel A and D), scattering efficiency (SE, panel B and E), and overall detection efficiency (ODE, panel C and F) for PSL, ammonium nitrate ( $\text{NH}_4\text{NO}_3$ ) and sodium chloride (NaCl) salt particles as a function of mobility diameter,  $d_m$ . Aerosol particles in this study were generated from a nebulizer and size-selected by DMA. In panel (B) and (E), optical counting efficiencies (OCE) for PSL and ammonium sulphate ( $(\text{NH}_4)_2\text{SO}_4$ ) at the detection beam from the study by Zawadowicz et al. (2017), corresponding to the SE defined in this study, are plotted for comparison. In panel (C) and (F), ODE for PSL and salt particles from other studies (Gemayel et al., 2016; Marsden et al., 2016; Zawadowicz et al., 2017) are plotted for comparison. In this figure, dashed lines are used only for guiding the eyes.

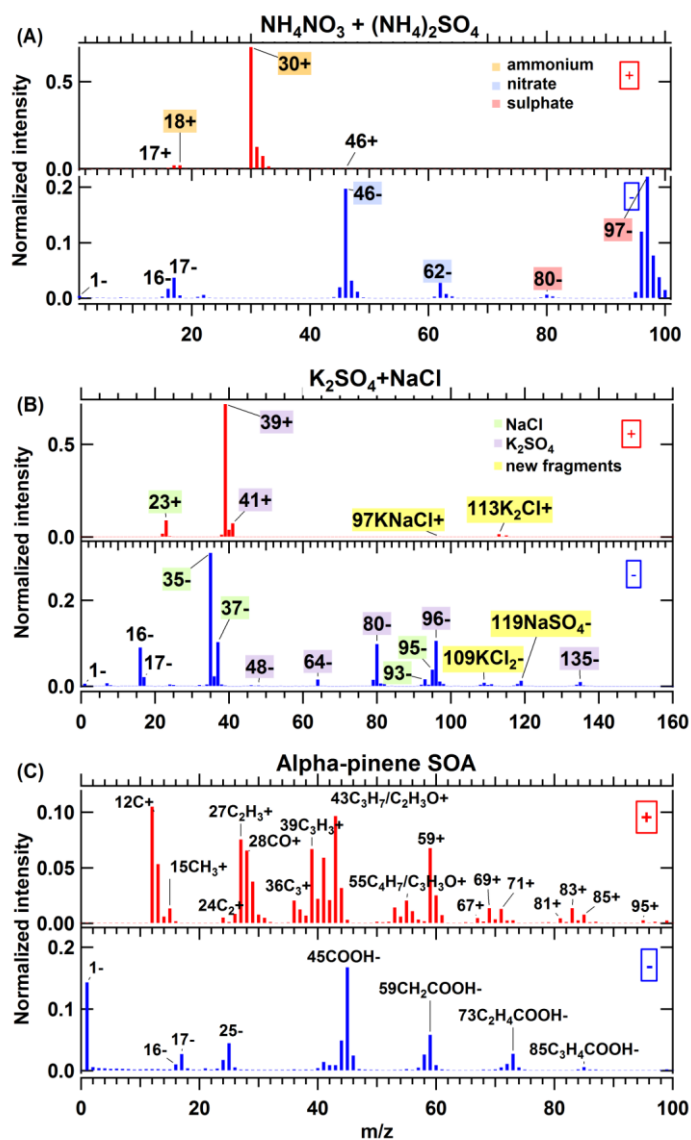




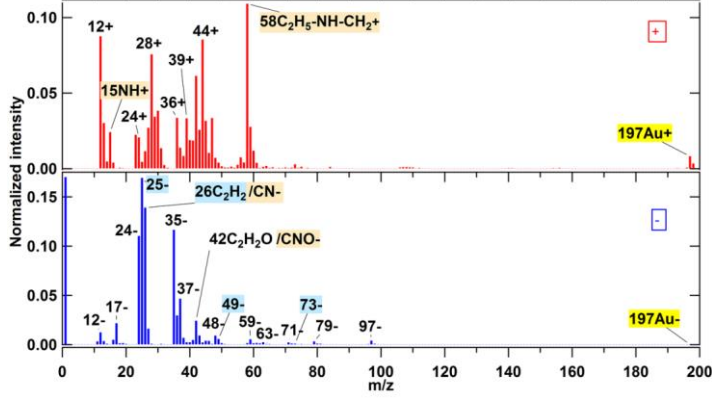
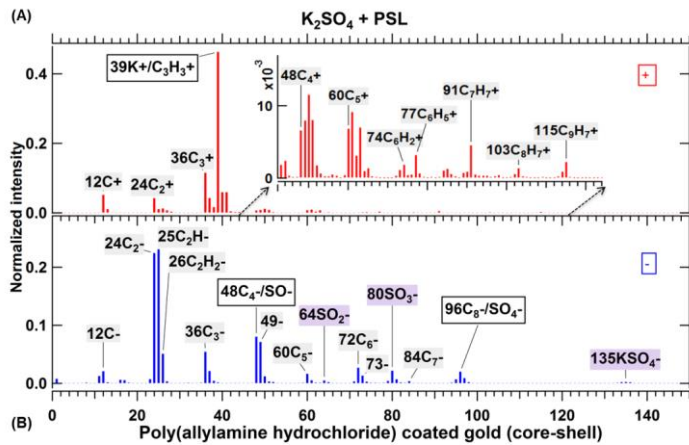
876

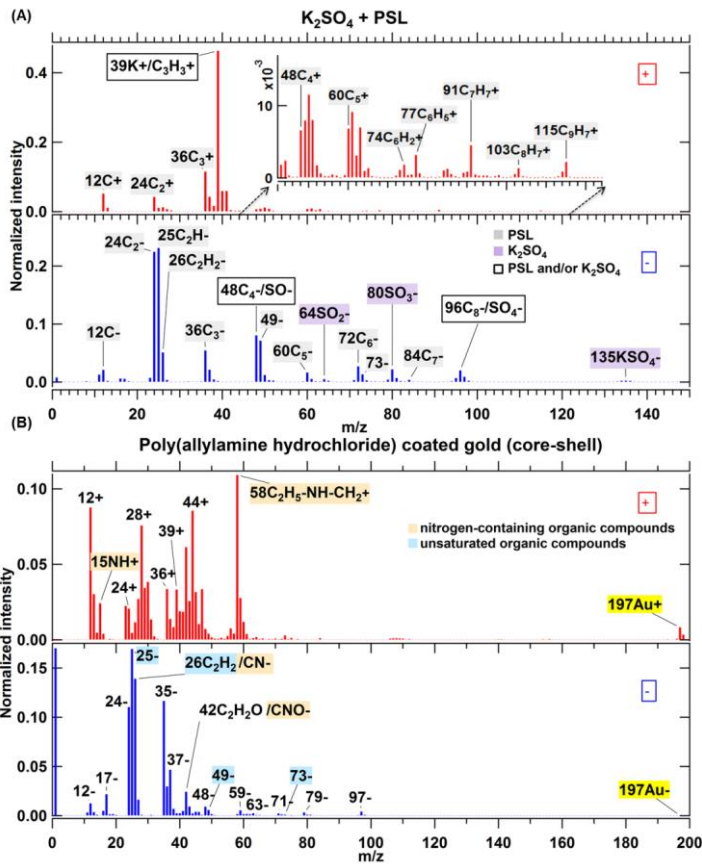
877 Figure 3: Average mass spectra for pure compound aerosol particles: (A)  $\text{NH}_4\text{NO}_3$  (dva=1160 nm), 497 single spectra averaged, (B)  
 878  $\text{K}_2\text{SO}_4$  (dva=1465 nm), 300 single spectra averaged, and (C) oxalic acid particles (dva=1081 nm), 736 single spectra averaged.



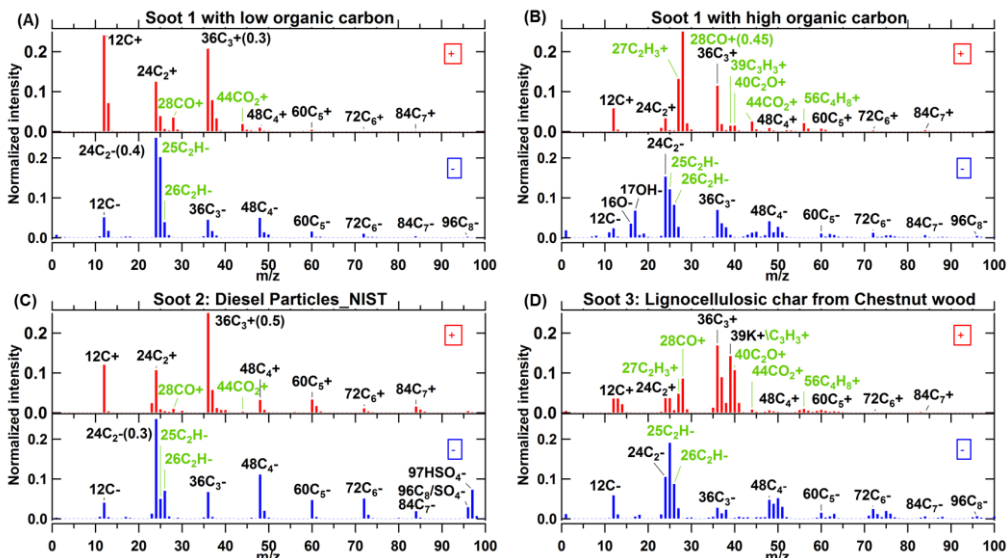


880  
 881 Figure 4: Average mass spectra for particles of internal mixtures of (A)  $\text{NH}_4\text{NO}_3$  and  $(\text{NH}_4)_2\text{SO}_4$ , (454 single spectra averaged and (B)  $\text{NaCl}$  and  $\text{K}_2\text{SO}_4$ , ( $d_{va} = 1375$  nm), 259 single spectra averaged as well and (C) secondary organic aerosol (SOA) particles from  $\alpha$ -pinene ozonolysis, which was performed in the APC chamber, then the resulting particles were transferred into the AIDA chamber at 263 K and 95% RH,  $d_{va} = 505$  nm, 1938 single spectra averaged. In panel (A), red, blue and orange label shadings represent fragments of sulphate, nitrate and ammonium, respectively. In panel (B), green and purple label shadings represent fragments from  $\text{NaCl}$  and  $\text{K}_2\text{SO}_4$  components (see section 3.2.1) in the mixed particles, respectively; yellow label shadings represent fragments only in the internal mixture of  $\text{NaCl}$  and  $\text{K}_2\text{SO}_4$ . In panel (C), labels with blue text represent fragments of organic acids.



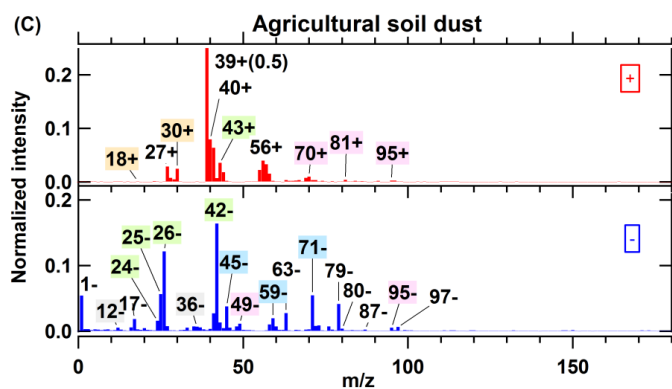
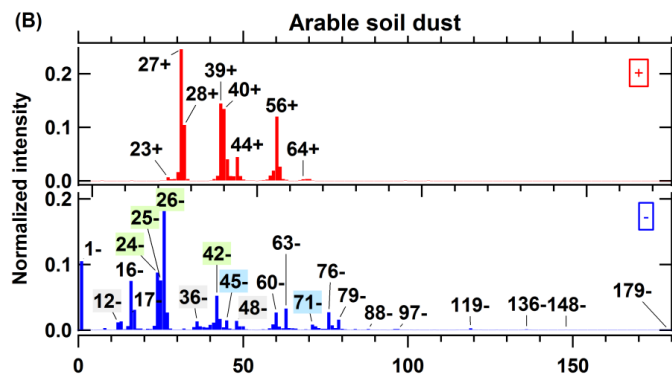
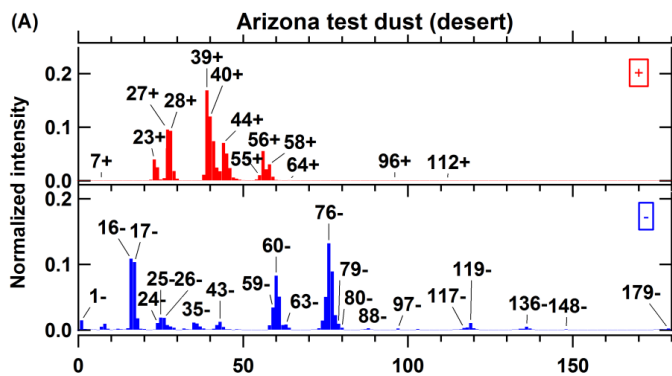


889  
 890 Figure 5: Average mass spectra for core-shell particles of (A) PSL coated with K<sub>2</sub>SO<sub>4</sub>, d<sub>va</sub>= 805 nm, 609 single spectra averaged, and  
 891 (B) poly(allylamine hydrochloride) coated gold (Au) particles with geometric 300 nm gold core and 50 nm thick organic shell, 417  
 892 single spectra averaged. In panel (A), grey and purple label shadings represent the fragments arising from pure PSL and pure K<sub>2</sub>SO<sub>4</sub>  
 893 components, respectively; box labels represent the fragments with contributions from core and shell compounds. In panel (B)  
 894 orange and blue label shadings represent the fragments arising from nitrogen-containing and unsaturated organic compounds, respectively,  
 895 and yellow label shadings represent gold.



896  
897  
898  
899  
900  
901

Figure 6: Average mass spectra for soot particles with (A) high elemental carbon (EC), low organic carbon (OC) content and (B) low EC and high OC from combustion of propane in a soot generator and transferred to a stainless steel cylinder of ~0.2 m<sup>3</sup> volume, as well as soot particles of (C) diesel particles (NIST) and (D) lignocellulosic char from Chestnut wood. In panel (A) and (C), the numbers in brackets beside peak 36<sup>+</sup> and 24<sup>+</sup> are the exact intensity values for them. The OC signatures are labeled in green. The numbers of spectra averaged for each spectrum are 617 (A), 347 (B), 533 (C) and 390 (D).



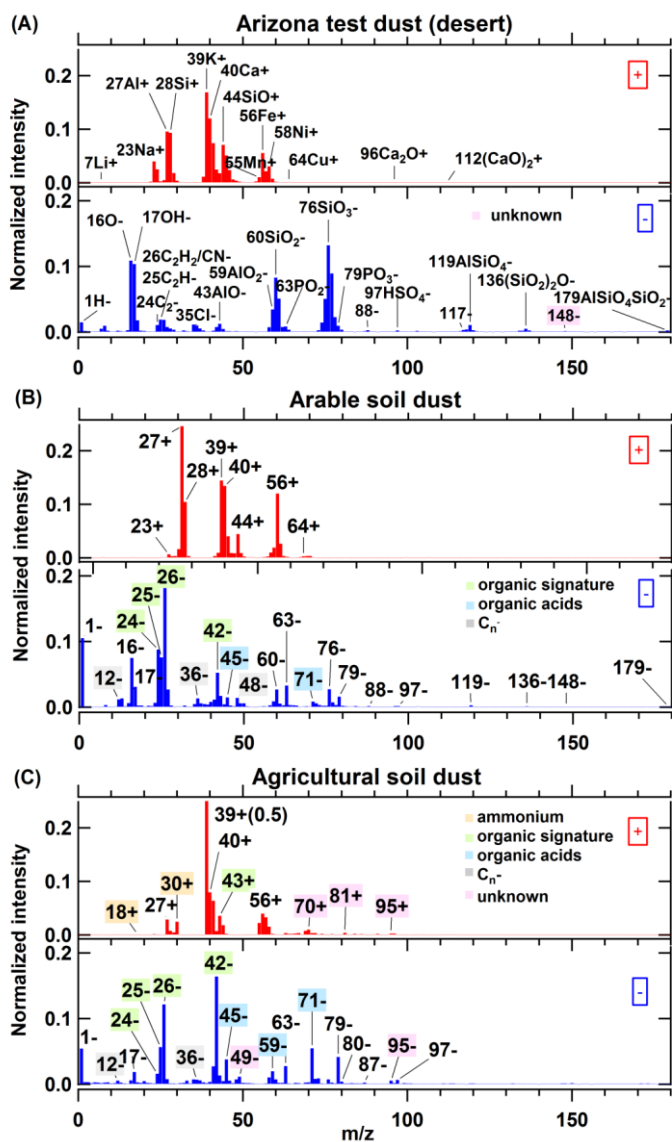
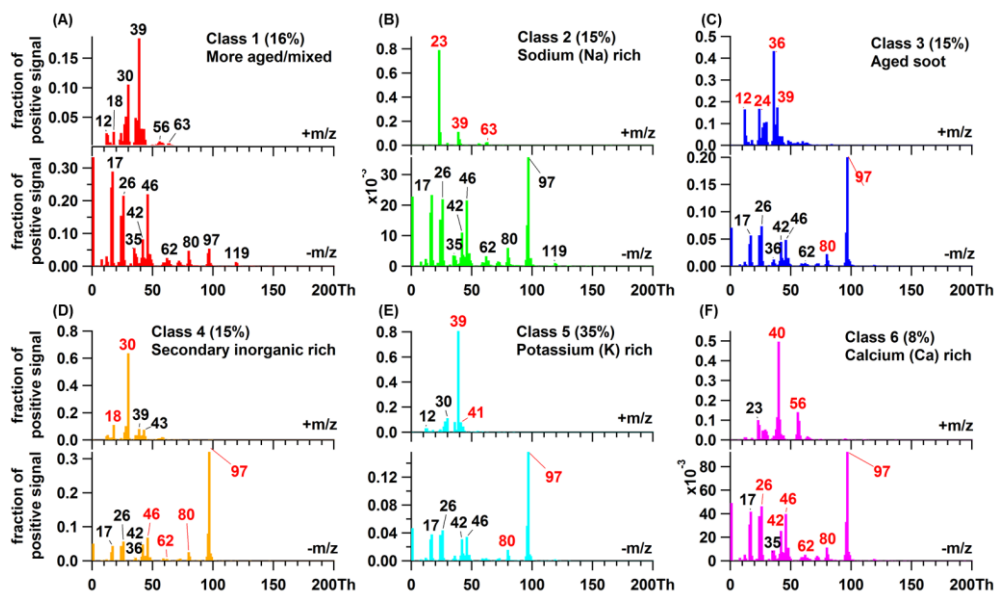


Figure 7: Average mass spectra for particles of complex mixtures: (A) Arizona test dust (desert dust), directly sampled into the LAAPTOF from a shaken bottle (B) arable soil dust, collected from Gottesgabe in Germany, was dispersed by a rotating brush generator and injected via cyclones into the AIDA chamber at 256 K and 80% RH, and (C) agricultural soil dust, collected from harvesting machines after rye and wheat harvest, were generated by using the same method as (B). For panel (B) and (C), fragments labelled in green represent more intensive organic signatures in soil dust particles; grey labels represent EC patterns; blue labels represent organic acids; orange labels represent ammonium salts; red labels represent unknown fragments. The numbers of spectra averaged for each spectrum are 261 (A), 583 (B), and 286 (C).



911

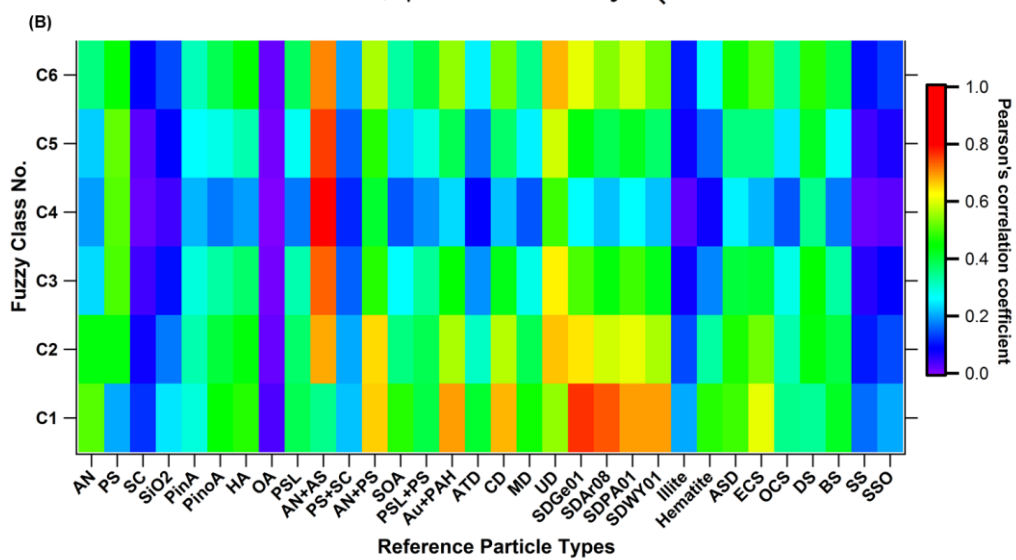
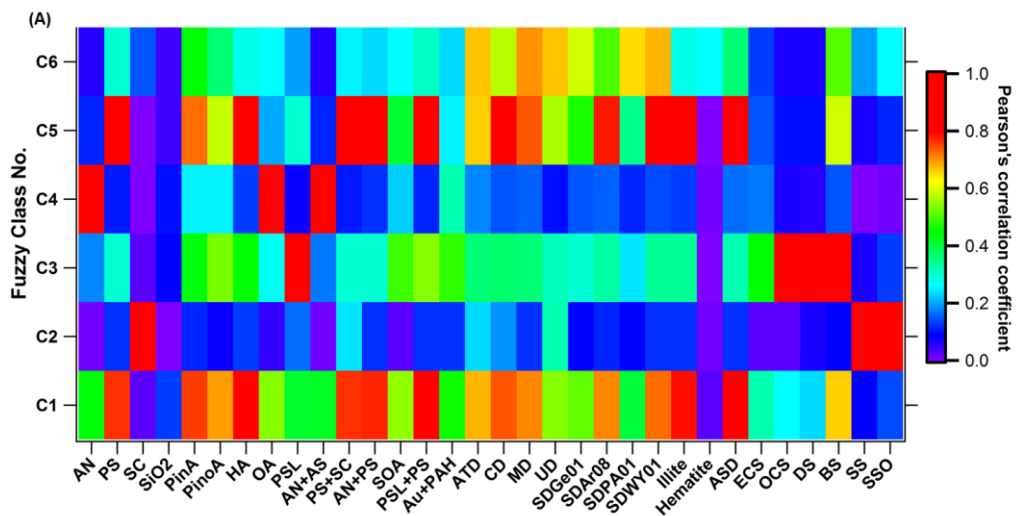
912

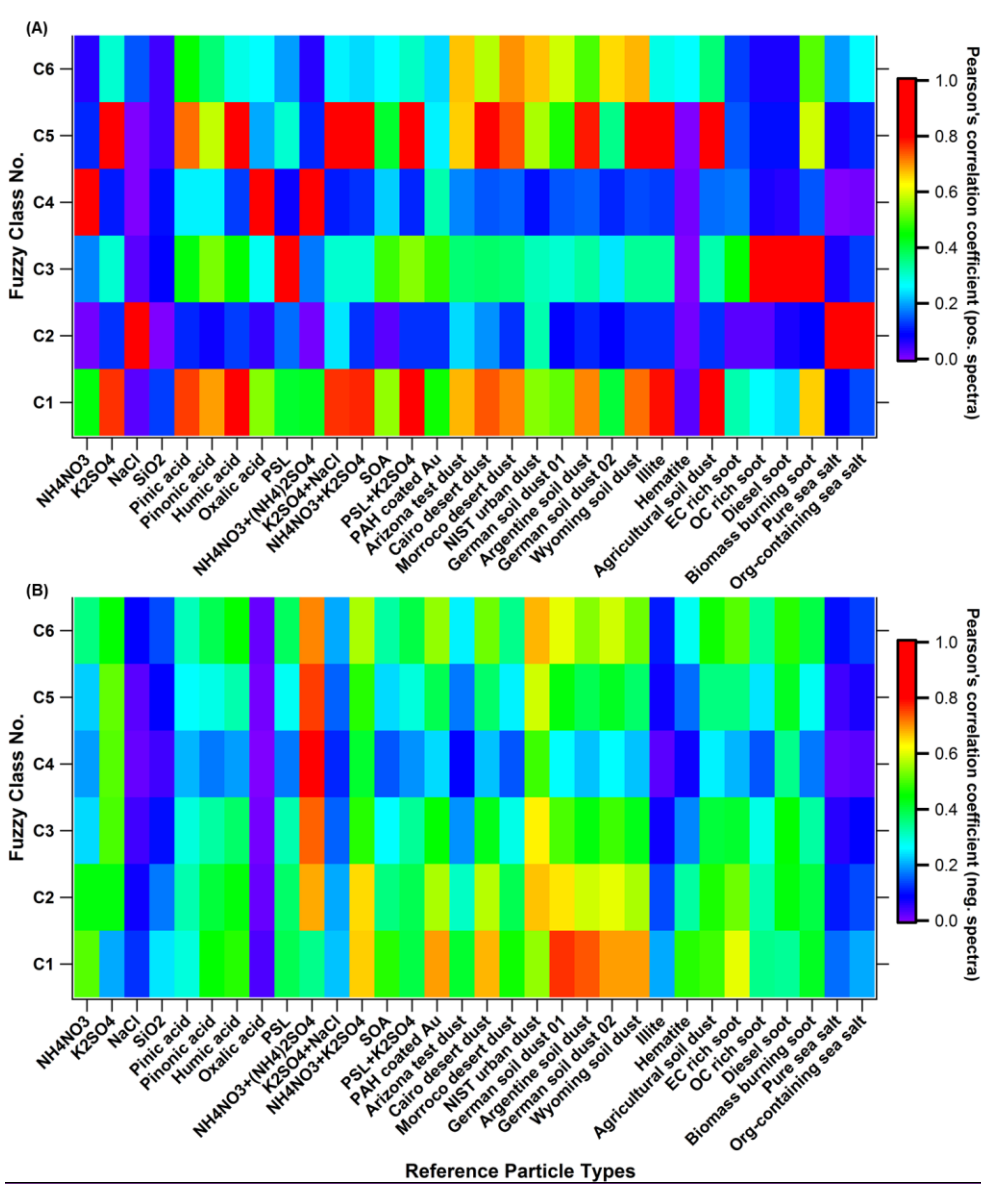
913

914

915

Figure 8: Mass spectra for six classes of particles measured on July 29<sup>th</sup>, 2016 during the field campaign TRAM01, based on classification according to Fuzzy c-means algorithm. The percentage in each pair of spectra (A to F) gives us information about the similarity of the total aerosols to different classes. The red tags represent the signatures for each typical class, but there is no red tag in spectra B, since this class is more aged particles that containing signatures for different classes. Mean particle size:  $d_w (676 \pm 165)$  nm.





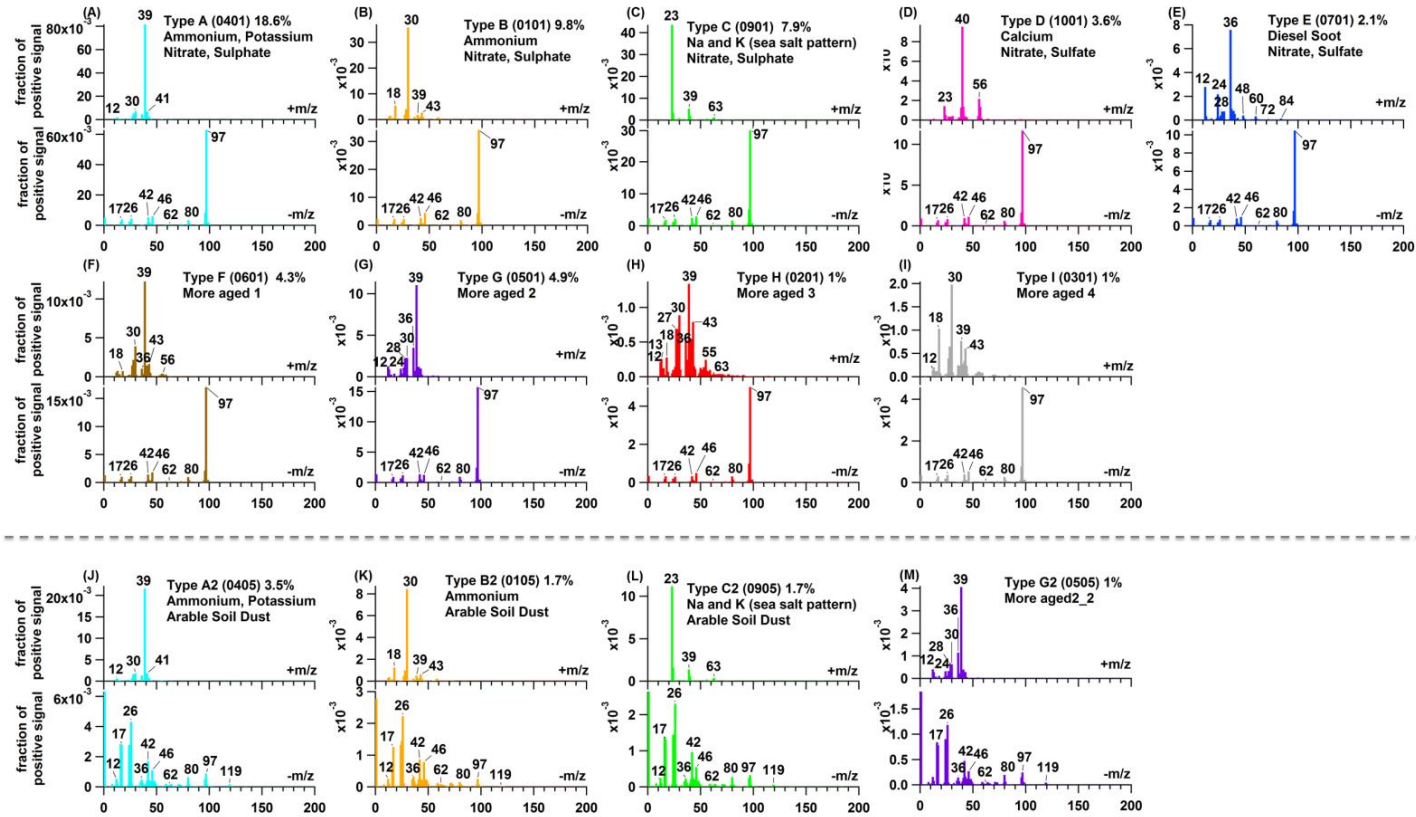
917  
 918 Figure 9: Correlation between Fuzzy classification results (6 classes, C1 to C6) and laboratory-based reference spectra. Panel (A) and  
 919 (B) are the correlation results for the positive and negative spectra, respectively. AN is short for ammonium nitrate, PAH is short for  
 920 poly(allylamine hydrochloride), PS-potassium sulphate, SC-sodium chloride, PinA-pinic acid, Pino-pinonic acid, HA-humid acid, OA-  
 921 oxalic acid, ATD-Arizona test dust, CD-Cairo dust, MD-Morocco dust, UD-urban dust, SDGe01 and SDPA01-soil dusts sampled at two  
 922 sites from Germany, SDAr08-soil dust from Argentina, SDWY01-soil dust from Wyoming in USA, ASD-agricultural soil dust, ECS-  
 923 EC rich soot1, OCS-OC rich soot1, DS-diesel soot, BS-biomass burning soot, which is the lignocellulosic char from Chestnut wood.

924 SS-pure sea salt, SSO-sea salt with organics.

Formatiert: Keine

**Formatiert:** Links: 2,36 cm, Rechts: 0,99 cm, Oben: 1,65 cm, Unten: 1,65 cm, Breite: 27,94 cm, Höhe: 21,59 cm

Formatiert: Standard, Block, Zeilenabstand: einfach



926  
927  
928  
929

Figure 10: Mass spectra for 13 different types of particles measured on July 29<sup>th</sup>, 2016 during the field campaign TRAM01, based on the classification according to laboratory-based reference spectra. The 4-digits codes in the brackets represent particle types (e.g. refer to Table S3 Table S2). The % values are the particle number fractions. For panel A to E and J to L, there are two lines for the names, the first and second lines correspond to the highly correlated positive and negative references, respectively.